

THESIS APPROVAL SHEET

Title of Thesis: A study of the impact of numerical dissipation on meso-scale simulations of

hurricane intensification with observational heating

Name of Candidate: Md Badrul Hachadrh1@umbc.edu

Master of Science 2022

Graduate Program: Mechanical Engineering

Thesis and Abstract Approved:

Meilin Yn Stephen Guimond

Meilin Yu Stephen Guimond

mlyu@umbc.edu sguimond@umbc.edu

Associate Professor Associate Research Professor

Mechanical Engineering Joint Center for Earth Systems Technology

NOTE: *The Approval Sheet with the original signature must accompany the thesis or dissertation. No terminal punctuation is to be used.

MD BADRUL HASAN

+1-443-453-4592 \prim mdbadrh1@umbc.edu \prim Halethorpe, Maryland, USA

EDUCATION

University Of Maryland, Baltimore County (UMBC)

January, 2019 - Present

Ph.D. in Mechanical Engineering

Department of Mechanical Engineering

University Of Maryland, Baltimore County (UMBC)

Expected December, 2022

M.S. in Mechanical Engineering

Department of Mechanical Engineering

Thesis Title: A study of the impact of numerical dissipation on meso-scale simulations of hurricane intensification with observational heating

Committee: Dr. Meilin Yu, Dr. Stephen Guimond, Dr. Belay Demoz

Bangladesh University of Engineering and Technology (BUET)

2013 - 2017

B.Sc. in Mechanical Engineering

Department of Mechanical Engineering

TECHNICAL STRENGTHS

Programming Languages Python, Matlab, Fortran

Modeling and Analysis AutoCad, Solidworks, Ansys, COMSOL

Software & Tools MS Office, Tecplot

WORK EXPERIENCE

Computational Mechanics Laboratory, UMBC

January, 2020 - Present

Graduate Research Assistant

· Working as a graduate research assistant with Dr. Meilin Yu, on developing machine learning based model development of back-scatter admitting sub-grid-scale (SGS) processes.

Joint Centre for Earth Systems Technology (JCET), UMBC Graduate Research Assistant

January, 2020-June, 2022

· Worked as a graduate research assistant with Dr. Stephen Guimond, on comparing the numerical dissipation of different weather prediction models like WRF and NUMA.

University Of Maryland, Baltimore County (UMBC) Graduate Teaching Assistant

January, 2019 - Present

· Working as a graduate teaching assistant for ENME-432L, Fluids/Energy Lab with Dr. Meilin Yu. Also worked as graduate teaching assistant for ENME-423, HVAC Design with Dr. James Baughan.

Khulna Power Company Ltd. (KPCL), Khulna, Bangladesh

February, 2017

Industrial Trainee

· One month training program in the first Independent Power Producer (IPP) of the country with hands on experience in Plant Operation, Fuel oil system, Lube oil system, Charge air and Exhaust gas system, Fire fighting system.

ABSTRACT

Title of dissertation: A STUDY OF THE IMPACT OF

NUMERICAL DISSIPATION ON MESO-SCALE SIMULATIONS OF HURRICANE INTENSIFICATION WITH OBSERVATIONAL HEATING

Md Badrul Hasan, Master of Science, 2022

Dissertation directed by: Dr. Meilin Yu

Department of Mechanical Engineering

Dr. Stephen Guimond

Joint Center for Earth Systems Technology

Numerous aspects of human existence, both material and immaterial, can be disrupted by a hurricane. In this work, the computational fluid dynamics of hurricane rapid intensification (RI) are studied by running idealized simulations with two different codes: a community-based, finite-difference/split-explicit model (WRF) and a spectral-element/semi-implicit model (NUMA). Rapid intensification is what RI stands for, how a hurricane gets stronger quickly. The main goal of this study is to find out how implicit numerical dissipation (IND) affects the energy of the vortex's response to heating, which describes the fundamental dynamics of the hurricane RI process. The heating that is taken into account here is derived from data. These observations include four-dimensional, fully nonlinear, latent heating/cooling rates estimated using airborne Doppler radar readings acquired during RI in a hurricane. The results show that WRF has more IND than NUMA, with a decrease

in several intensity parameters, such as (1) the time-integrated mean kinetic energy values that WRF predicts are 20% lower than those that NUMA predicts and (2) the peak, localized wind speeds that WRF predicts are 12 meters per second slower than those that NUMA predicts. To make a time series of intensity similar to NUMA, the eddy diffusivity values in WRF need to be less than those in NUMA by about 50%.

Kinetic energy budgets reveal that the pressure contribution is the primary cause in the model variations, with WRF generating an average $\sim 23\%$ lower vortex energy input. The IND is associated with the low-order spatial discretization of the pressure gradient in WRF. In addition, the mean contribution of the eddy transport term to the vortex intensification is determined to be $\sim 20\%$ positive. These findings have significant implications for the academic and operational forecasting communities that employ WRF and similar numerical methods.

A STUDY OF THE IMPACT OF NUMERICAL DISSIPATION ON MESO-SCALE SIMULATIONS OF HURRICANE INTENSIFICATION WITH OBSERVATIONAL HEATING

by

Md Badrul Hasan

Dissertation submitted to the Faculty of the Graduate School of the University of Maryland, Baltimore County in partial fulfillment of the requirements for the degree of Master of Science, 2022

Advisory Committee:

Dr. Meilin Yu, Chair/Advisor

Dr. Stephen Guimond, Co-Chair/Co-Advisor

Dr. Belay Demoz

© Copyright by Md Badrul Hasan 2022

Acknowledgments

I want to thank my advisors, Dr. Meilin Yu and Dr. Stephen Guimond, for providing their patience, invaluable insight, and guidance through this journey for the past several years. I am also thankful to Dr. Belay Demoz for serving on my master's committee and for meaningful feedback. I want to acknowledge Dr. Frank Giraldo and Dr. Sohel Reddy from the Naval Postgraduate School for their help in understanding NUMA. I thank NOAA/HRD for collecting and processing the raw radar data used in this thesis work. Thanks to the UMBC Mechanical Engineering Department's guidance, graduate assistant support, and knowledge. The hardware used for the computational studies in this work is part of the University of Maryland, Baltimore County (UMBC) High-Performance Computing Facility (HPCF). The U.S. National Science Foundation supports HPCF through the MRI program (grant nos. CNS-0821258, CNS-1228778, and OAC-1726023) and the SCREMS program (grant no. DMS-0821311), with substantial additional support from UMBC.

I gratefully acknowledge the sources that funded my master's research, the National Science Foundation (NSF) under grant AGS-2121366. Additional support was provided by a UMBC Strategic Awards for Research Transitions (START) grant to Dr. Stephen Guimond.

Lastly, I would like to thank my family and friends for all their love, support, and encouragement.

Table of Contents

List of Tables	iv
List of Figures	v
List of Abbreviations	vii
1 Introduction 1.1 Background - Hurricane Formation	1 1 3 8
2.1.2 The NUMA Model	9 9 9 11 13
3.1 Time Series and Structure of Windspeed	22 22 30 41
4.1 Summary	48 48 52
Bibliography	54

List of Tables

2.1	Numerical methods, boundary conditions and sub-grid scale diffusion	
	used in WRF and NUMA simulations	18
2.2	Coefficients for the horizontal and vertical viscosity polynomial fits	2

List of Figures

1.1 1.2	Formation of a Hurricane	3
2.1	Axisymmetric tangential velocity (m/s) in the radius-height plane for the initial vortex used in each model	15
2.2	Three-dimensional iso-surfaces of latent heating (red; $100 \ K/h$) and cooling (blue; $-100 \ K/h$) retrieved from airborne Doppler measurements in regidus intensifying Harrisona Cuillernes (1997)	17
2.3	ments in rapidly intensifying Hurricane Guillermo (1997) Eddy viscosity (m^2s^{-1}) values output from the WRF 3D TKE scheme	17
4.0	at 6 h and 0.5 km height (left panel) and 9.8 km height (right panel).	19
2.4	Maximum eddy viscosity values from the 3D TKE scheme in WRF	
	as a function of height	20
3.1	Time series of maximum windspeed for the control WRF and NUMA	
0.1	simulations.	23
3.2	Time series of maximum azimuthal mean windspeed for the control	
	WRF and NUMA simulations as well as higher horizontal resolution	
	WRF simulations at 1 km and 0.5 km.	24
3.3	Time series of azimuthal mean kinetic energy averaged over the eye-	
	wall ($\sim 10 - 50 \ km$ radius) and height ($\sim 0.19 - 1.5 \ km$) for the control WRF and NUMA simulations.	25
3.4	Horizontal wind speed perturbations (m/s) and differences (m/s) at	20
	4 h for WRF and NUMA at $0.19 km$ and $4.83 km$ height levels.	
	Panels (e) and (f) show the differences (NUMA - WRF) at the same	
	corresponding height levels	27
3.5	The same as in Fig. 3.4, only showing the $0.19 km$ height level at 5	
	h and 6 h in WRF in panels (a) and (b), respectively and NUMA in	
	panels (c) and (d). Panels (e) and (f) show the differences (NUMA -	0.0
	WRF) at the same corresponding time periods	28

3.6	Horizontal wind speed differences (NUMA - WRF) in (m/s) at 0.19	
	km height at 4 h , 5 h and 6 h for the control NUMA simulation and	
	varying horizontal grid spacing in WRF (2 km, 1 km and 0.5 km).	
	Each panel is identified according to the row (WRF resolution) and	
	column (time period) as denoted on the figure	29
3.7	Time series of azimuthal mean kinetic energy budget tendencies from	
	both models after averaging	33
3.8	Time series of the summation of terms that control the time tendency	
	of azimuthal mean kinetic energy on the RHS of Eqn (3.9). The	
	dashed lines represent all terms on the RHS of Eq. (3.9), while the	
	solid lines include only the M, E and P terms. After summation, the	
	fields are averaged as is done in Fig. 3.7	35
3.9	Panel (a) shows height-averaged, observational heating inputs to mod-	
	els around 4 h. Panels (b) and (c) demonstrate WRF's radial and	
	tangential horizontal pressure gradient contributions (m^2s^{-3}) to ki-	
	netic energy. Panels (d) and (e) are NUMA versions of (b) and (c).	
	Panels (b)–(e) are 4 h into the simulations	38
3.10	Panel (a) show the height-averaged, observational heating inputs to	
	the models for time period $\sim 5.0 \ h$. All other panels are the same as	
	in Figure 3.9, only for 5 h into the simulations	40
3.11	18-h simulations' idealized heating perturbations (K/h) . Panels (a)	
	and (b) depict horizontal and vertical cross sections at $z = 5$ km and	4.4
0.10	x = 0 km, respectively	41
3.12	Time series of maximum azimuthal mean windspeed for the 18 hour	40
ก 1ก	WRF and NUMA simulations	42
3.13	Horizontal wind speed perturbations (m/s) in each model and differ-	
	ences (NUMA - WRF) in (m/s) at 0.19 km height for the 18-hour	49
9 1 1	simulations at $10.5 h$, $15 h$, and $17 h$	43
5.14	Time series of maximum azimuthal windspeed difference for the 18 hours WRF and NUMA simulations	16
	HOUIS WAF AND NUMA SHIDDAHORS	46

List of Abbreviations

NOAA National Oceanic and Atmospheric Administration

NOAA/HRD NOAA Hurricane Research Division CFD Computational Fluid Dynamics

RI Rapid Intensification

WRF Weather Research and Forecasting

NUMA Nonhydrostatic Unified Model of the Atmosphere

IND Implicit Numerical Dissipation

SGS Sub-grid-scale

CG Continuous Galerkin
DG Discontinuous Galerkin

KE Kinetic Energy

TKE Turbulent Kinetic Energy
CG-SEM CG Spectral Element Method
LF2 Second Order Leapfrog Scheme
RMW Radius of Maximum Wind

h Hours km Kilometer

LES Large Eddy Simulations

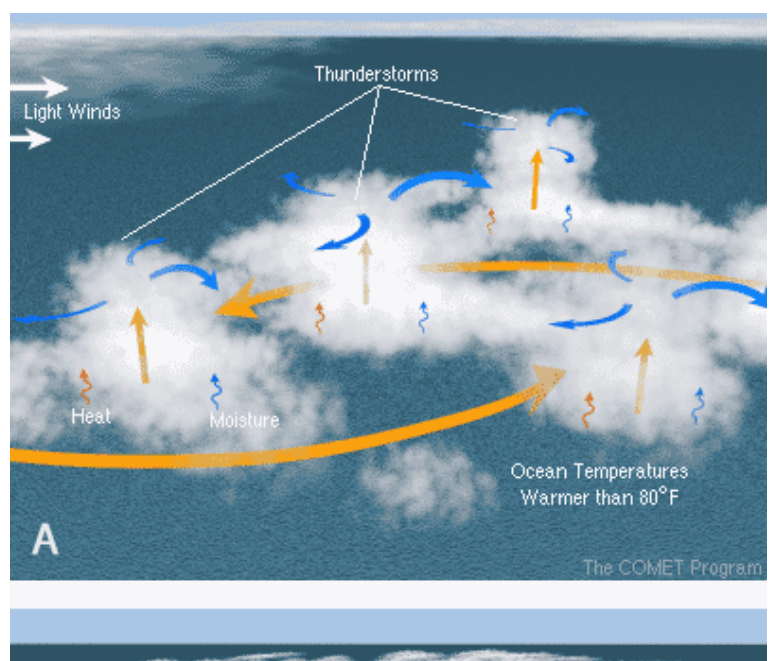
ML Machine Learning

Chapter 1: Introduction

1.1 Background - Hurricane Formation

Tropical cyclones include hurricanes and tropical storms. Low-pressure systems form in the tropics or subtropics and have things like thunder and lightning happen in these. In the Atlantic and northeastern Pacific Oceans, stronger storms are called "hurricanes," and in the northwestern Pacific Ocean, they are called "typhoons." "Tropical depressions" or "tropical storms" are the names for less powerful tropical cyclones. The National Hurricane Center puts hurricanes into groups based on how fast their winds are. A Category 1 hurricane is a storm with winds over 74 mph. "Major hurricanes" are storms with winds of more than 111 miles per hour (Category 3 or higher). The wind speed is just one of many things that affect how bad a hurricane is. Other things to consider are the storm's track (where it hits land), size, storm structure, amount of rain, length of time, and how vulnerable the area is.

Recent storms, such as Hurricane Michael, which obliterated the Florida panhandle in 2018, and Hurricane Harvey, which flooded parts of Texas in 2017, demonstrate the devastation these systems can cause even in the modern era. The record-breaking hurricane season in the Atlantic Ocean in 2020 will also serve as an example.



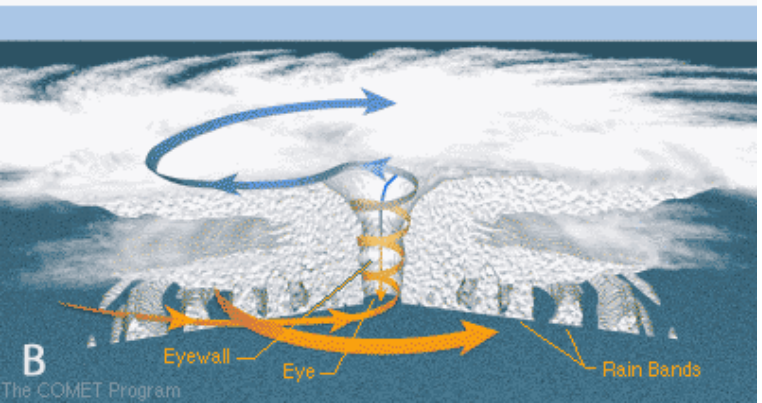


Figure 1.1: For a hurricane to form, there must be thunder, warm water in the ocean, and light winds (A). Once it's formed, a hurricane is made up of big rotating bands of rain and a center of clear skies called the eye. The fast winds of the eyewall surround the eye (B).[Source- COMET/UCAR]

Unfortunately, new research suggests that as the climate system continues to warm, severe hurricanes will likely grow more regular, produce more flooding rainfall, and stay longer even after landfall [1–3]. This is all due to the warming of the climate system. As a result, hurricanes will likely place increasing stress on many sectors of

society in various countries across the globe.



Figure 1.2: Before (top) and after (bottom) Hurricane Ivan hit the coast in September 2004, these homes were in Orange Beach, Alabama, which is on a barrier island.[Source- USGS]

1.2 Motivations

Dynamical model predictions of a hurricane's path, intensity, storm surge, and rainfall can save lives and prevent billions of dollars in damage by allowing more time to be spent preparing for the disaster and evacuating vulnerable areas. However, substantial forecast errors remain a problem in operational predictions of hurricane intensity, remarkably rapid intensification (RI) [4, 5]. According to DeMaria et al. [6], from 1991 and roughly 2015, neither one of the deterministic models could accurately predict RI. While both dynamical and statistical models have shown promise in RI forecasting since 2015, considerable under-prediction or low bias in RI cases persists even now [7].

The vortex response to heating in convective clouds drives the rise in kinetic energy in hurricane intensification and RI [8], and the source of moist enthalpy flow originates from the thermodynamic disequilibrium between the ocean and the atmospher [9]. The boundary layer is the most crucial region for energy dissipation, and it does so primarily via surface friction and a hierarchy of turbulent eddies at different scales. Recent studies, however, have revealed that the hurricane boundary layer contains coherent turbulent structures that can "backscatter" radar signals "the transmission of energy to bigger scales [10]. Energy dissipation can also happen implicitly in numerical models as a result of the algorithms used to solve the fluid-flow equations (what is known as "implicit numerical dissipation") implicitly (without filters) or explicitly (with filters). Low-order spatial and temporal discretizations of the governing equations can lead to implicit numerical dissipation. In particular, numerical dissipation error can be significantly reduced by using high-order (e.g., fifth) or centered schemes rather than lower-order (e.g., second) or upwind-biased spatial discretizations of the advective components [11, 12].

Errors caused by excessive dissipation can quickly propagate through the sys-

tem; hence it is preferable to have as little numerical dissipation as possible when dealing with highly nonlinear computational fluid dynamics situations like hurricanes. To better understand the role of sub-grid scale models in describing turbulent channel flow, Kravchenko et al., [13] looked into numerical errors in spectral and finite difference codes. They showed that low-order (e.g., second) finite-difference schemes substantially attenuate the energy spectrum at high wave numbers and that the contribution of the sub-grid scale model is negligible. Results from large eddy simulations and the efficiency of the sub-grid size model were improved by raising the order of the finite-difference approximations. For shock/turbulence interaction simulations, Larsson et al. [14] discovered that keeping numerical dissipation small was crucial, especially for coarse resolution simulations when the fields are underresolved, and a sub-grid model is needed. In this study, we apply this setup to mesoscale atmospheric modeling. The computational dissipation was significant enough in the under-resolved simulations [14] to reduce or eliminate the smallerscale motions on the grid and from the sub-grid model. It has been demonstrated that for large eddy simulations, implicit numerical dissipation can imitate the effects of a sub-grid turbulence model [15]. So, only some numerical dissipation is good for the outcome of a simulation. Further, in the high wave-number regions of the flow field where the dissipation is active, the employment of some numerical dissipation (in addition to fake viscosity) can assist control the impacts of numerical dispersion errors.

In comparison to low-order (i.e., the order of accuracy equal to or smaller than two) methods and other high-order methods, including finite volume/difference schemes, continuous Galerkin (CG), and discontinuous Galerkin (DG) numerical methods have several distinctive qualities. They are 1) highly scalable and efficient on massively parallel supercomputers, such as those accelerated by Graphics Processing Units (GPUs); 2) able to achieve arbitrary high-order discretization for all spatial derivatives; and 3) possessing low dissipation and dispersion errors for turbulent flows with highly disparate spatial and time scales [16, 17]. Because of their superior numerical features, high-order CG and DG approaches are appealing for studying hurricanes. High-order numerical techniques are superior to low-order methods for solving flow problems with a low Reynolds number at The International Workshop on High-Order CFD Methods [18]. In contrast, high-order numerical systems can struggle with excessive grid-scale noise, aliasing, and stability when simulating under-resolved problems that call for a sub-grid turbulence model and problems with discontinuities [19–21]. When these occur, the simulation may fail, or the simulated flow may be inaccurate. De-aliasing methods [20, 22–25], localized artificial viscosity [26, 27], and others have been developed to combat these issues. Stabilizing flow simulations can be accomplished with the use of limiters [28–30]. For this research, we employ a hybrid method, wherein we apply artificial viscosity based on results from a turbulent kinetic energy (TKE) sub-grid model for turbulent diffusion (further information on this may be found in Section 2.1.3).

When simulating squall lines, Takemi et al. [31] used the Weather Research and Forecasting (WRF) model. This finite difference-based code allows for high-order discretization of the advective (or flux divergence) elements exclusively [12]. The scientists discovered many noisy, grid-scale convective cells using a typical TKE

sub-grid model with a fifth-order, upwind-biased advection scheme. To avoid potentially detrimental effects on physical modes from using an explicit numerical filter, the authors of this study instead calibrated the TKE sub-grid model coefficient to generate wavelength-dependent convective structures with suitable energy densities. The significance of examining numerical dissipation was demonstrated by testing the addition of an explicit numerical filter and discovering that it had a far higher impact on the solutions than the sub-grid TKE model. A careful balance between signal and noise must be maintained to ensure the high precision and stability of a simulated flow.

Guimond et al. [32] revealed that implicit numerical dissipation could lead to substantial changes in system intensity among models due to the vortex response to simple, impulsive, asymmetric thermal anomalies. Compared to atmospheric research codes like HIGRAD and NUMA (Nonhydrostatic Unified Model of the Atmosphere), WRF had abnormally significant implicit numerical dissipation, which muted the intensity response from asymmetric thermal anomalies. Less numerical dissipation in HIGRAD and NUMA led to a more energetic reaction. The flux of inertia-gravity wave energy explains most of the variance in the pressure term, according to spectral kinetic energy budgets. In WRF, acoustic and inertia-gravity waves are called fast modes. This led to the recommendation that WRF's numerical dissipation was caused by its time integration scheme. Sensitivity experiments with NUMA time integration systems demonstrated energy and pressure term role variances.

1.3 Outline of Thesis

This work looks at how a tropical storm-like vortex reacts to time-dependent, 3-D observational heating calculated from airborne Doppler radar measurements in the RI of Hurricane Guillermo (1997). Chapter 2 presents a detailed description of the numerical models and simulation setup. We provide the WRF and NUMA models, vortex initialization and heating procedures, and eddy viscosity and diffusivity configuration.

Comparison of the wind field features, e.g., maximum and azimuthal mean wind speed and kinetic energy, from WRF and NUMA, is discussed in Chapter 3. This chapter also presents kinetic energy budget analyses to explain the wind field disparity between WRF and NUMA. Similar features for more extended period simulations are studied in section 3.3.

Important implications of this work in the hurricane research and operational fields are given in Chapter 4. Future work is discussed in this Chapter 4.2.

Chapter 2: Methodology

2.1 Description and Setup of Numerical Models

Guimond et al. [32] provides a complete introduction to the governing equations and numerical methods employed in the WRF-ARW (after this WRF) and NUMA models. In Table 2.1, we provide a quick reference of the numerical methods, boundary conditions, and sub-grid size diffusion parameters utilized in each model for completeness.

2.1.1 The WRF Model

The non-hydrostatic, compressible Euler equations are solved conservatively in the WRF model using the η mass vertical coordinate [12,33]. In post-processing, all variables are interpolated to conventional height levels for comparisons with NUMA. The variations between η levels and height are negligible in these idealized simulations. Using a Laplacian operator for explicit diffusion and η as the vertical coordinate, the simplified model equations for a dry environment can be written as follows:

$$\frac{\partial mu}{\partial t} + \nabla \cdot (m\mathbf{u}u) = -\frac{m}{\rho} \frac{\partial \hat{p}}{\partial x} + fmv + \nabla \cdot (m\mu\nabla u) \tag{2.1}$$

$$\frac{\partial mv}{\partial t} + \nabla \cdot (m\mathbf{u}v) = -\frac{m}{\rho} \frac{\partial \hat{p}}{\partial y} - fmu + \nabla \cdot (m\mu \nabla v)$$
 (2.2)

$$\frac{\partial mw}{\partial t} + \nabla \cdot (m\mathbf{u}w) = g\left(\frac{\partial \hat{p}}{\partial \eta} - \hat{m}\right) + \nabla \cdot (m\mu\nabla w) \tag{2.3}$$

$$\frac{\partial m\theta}{\partial t} + \nabla \cdot (m\mathbf{u}\theta) = S + \nabla \cdot \left(m\kappa\nabla\hat{\theta}\right) \tag{2.4}$$

$$\frac{\partial m}{\partial t} + \nabla \cdot (m\mathbf{u}) = 0. \tag{2.5}$$

u, v, and w are the three-dimensional velocities, m = m(x, y) is the column mass per unit area, θ is the potential temperature, ρ is the dry air density, \hat{p} is the perturbation pressure, f is the Coriolis parameter, g is gravity, μ is the eddy viscosity, κ is the thermal diffusivity and S is the heating rate source term. Variables with hats indicate hydrostatically balanced perturbations.

WRF uses a combination of finite-difference/finite-volume spatial discretization. A spatially staggered Arakawa C grid is used in horizontal and vertical directions, with velocities on cell faces and scalars at cell centers. Fifth-order, upwind-biased horizontal discretization and third-order vertical discretization are employed for nonlinear advective terms. We used these parameters but also evaluated even-ordered, less diffusive schemes (sixth-order and fourth-order in the horizontal and vertical dimensions, respectively). The discrepancies between even-ordered and odd-ordered schemes were minor (maximum values of \pm 0.5 \pm 1 m/s in the eyewall). The WRF model uses a split-explicit time integration approach to calculate acoustic and

gravitational wave modes with a small time step and advection with a larger time step [12,34,35]. Vertical modes are implicitly solved during the short period. Backward Euler is used to solving for the implicit solution. Third-order Runge-Kutta is used to integrate small- and large-time step equations. During Runge-Kutta time integration, small-time step findings correct large-time step computations. citeSkamarock-2008 for WRF information. To obtain minimally dissipative WRF solutions, we switched off explicit sixth-order numerical filtering, vertical velocity damping, divergence damping, and external mode damping. The above equations apply artificial viscosity at the model top and through Laplacian operators.

2.1.2 The NUMA Model

Different versions of the Euler equations can be implemented in the NUMA model [36,37]. To be compatible with Guimond et al. [32], however, we employ the non-conservative version, in which potential temperature is the thermodynamic variable [38,39]. Since the error resulting from the non-conservative set is substantially lower than the temporal error, it is not envisaged that the choice of a conservative or non-conservative equation set will make a significant difference. In NUMA, height z is employed as the vertical mass coordinate instead of the more familiar η . These are the governing equations:

$$\frac{\partial u}{\partial t} + \mathbf{u} \cdot \nabla u = -\frac{1}{\rho} \frac{\partial \hat{p}}{\partial x} + f v + \nabla \cdot (\mu \nabla u)$$
 (2.6)

$$\frac{\partial v}{\partial t} + \mathbf{u} \cdot \nabla v = -\frac{1}{\rho} \frac{\partial \hat{p}}{\partial y} - f u + \nabla \cdot (\mu \nabla v)$$
 (2.7)

$$\frac{\partial w}{\partial t} + \mathbf{u} \cdot \nabla w = -\frac{1}{\rho} \frac{\partial \hat{p}}{\partial z} - \frac{\hat{\rho}}{\rho} g + \nabla \cdot (\mu \nabla w)$$
 (2.8)

$$\frac{\partial \theta}{\partial t} + \mathbf{u} \cdot \nabla \theta = S + \nabla \cdot \left(\kappa \nabla \hat{\theta} \right) \tag{2.9}$$

$$\frac{\partial \rho}{\partial t} + \nabla \cdot (\rho \mathbf{u}) = 0 \tag{2.10}$$

The CG spectral element method (CG-SEM) is used to make Eqs. (2.6)-(2.10)spatially discrete [36, 39, 40]. State variables are represented by polynomial expansions using Lagrange basis functions of a given order, and the physical domain is partitioned into a collection of non-overlapping hexahedral elements. In discrete form, the continuous spatial derivatives are made by taking the derivatives of the polynomials that are close to the solutions. The state variables in each element are close to each other and placed at Legendre-Gauss-Lobatto points that are not all the same distance apart. In this study, we use fifth-order polynomial basis functions in all three dimensions of space. This gives us fifth-order accuracy for all spatial derivatives and is the same as what Guimond et al. [32] showed. Note that the stencil for all polynomial orders in NUMA is symmetric about the centroid of the element. This means that fifth-order polynomials do not have upwind-biased diffusion. The three-dimensional semi-implicit method and a second-order leapfrog scheme (LF2) with backward Euler off-centering are used to integrate time. With a coefficient of 0.2, a first-order Robert-Asselin time filter stabilizes the LF2 scheme. This gets rid of the computational mode. Our control simulations are part of the above description of NUMA. There are a few other ways to integrate time in NUMA, and we will show where sensitivity tests have been done. For more information about the

NUMA model, interested readers can look at this works [36, 39].

2.1.3 Details of Simulation Setup

We take a model hierarchy approach to study hurricane intensification. We first employ idealistic simulations utilizing various numerical techniques to establish a foundation of understanding and then add physics layers to advance this understanding into the whole regime. The CG spectral element method (CG-SEM) is used to determine whether there are variations in the model solutions to the numerical schemes that make up the dynamic core. Careful investigation has been done to ensure that WRF and NUMA are configured in a virtually identical manner. In addition, as will be shown in the following section, we have imposed several idealizations in physics to isolate the vortex's reaction to heating, which is the fundamental dynamics governing the intensification of hurricanes. As a result, it is not our intention to provide a detailed account of a particular incident.

The computational domain is $800 \ km$ horizontally and $20 \ km$ in length vertically. WRF uses $2 \ km$ horizontal grid spacing to match radar measurements used as forcing and to be consistent with Guimond et al. [32]. The initial model level is $167 \ m$ with $333 \ m$ vertical spacing up to the model top (60 levels). The NUMA grid has $80 \ elements$ in each horizontal direction and $12 \ elements$ in each vertical direction, along with fifth-order polynomials in all dimensions, to match WRF's horizontal and vertical grid spacing. These settings give NUMA element-averaged grid spacing of $2 \ km$ horizontally and $333 \ m$ vertically. The time step in each model is $2 \ seconds$.

Each model uses periodic boundary conditions in both horizontal directions. The computing domain has a gravity wave absorption zone (sine-squared function), with the WRF zone covering the top $4\ km$ with a small coefficient (0.00833) and the NUMA zone covering the top $1\ km$ with a big coefficient (1.0). Stability difficulties cause absorbing zone discrepancies. However, sensitivity tests demonstrate the results are not sensitive to these options. Each model applies the free-slip boundary condition at the bottom of the computational domain to deactivate surface fluxes and prevent a frictional boundary layer. These idealizations focus on the vortex dynamic response to forced heating. Four-dimensional latent heating/cooling rates from aerial Doppler radar observations compel the simulations without moisture.

Post-processing interpolates WRF and NUMA fields to a consistent, collocated grid at the above horizontal/vertical grid spacings. When processing the WRF results afterward, linear interpolation is used. Using the spectral element approach, the NUMA outputs are high-order interpolated using Lagrange polynomials. To facilitate interpolation, any hexahedral element in the physical space (x, y, z) can be translated into a standard space $(\alpha, \beta, \gamma) \in [-1, 1] \times [-1, 1] \times [-1, 1]$. This means that there are N+1 Legendre-Gauss-Lobatto points for any Nth-order standard hexahedral element, one in each of the α , β , and γ directions. The Lagrange polynomial basis $L_{IJK}(\alpha, \beta, \gamma)$, $I, J, K = 1, \ldots, N+1$, can be built with the tensor product

as

$$L_{IJK}(\alpha, \beta, \gamma) = \left(\prod_{i=1, i \neq I}^{N+1} \frac{\alpha - \alpha_i}{\alpha_I - \alpha_i}\right) \left(\prod_{j=1, j \neq J}^{N+1} \frac{\beta - \beta_j}{\beta_J - \beta_j}\right) \left(\prod_{k=1, k \neq K}^{N+1} \frac{\gamma - \gamma_k}{\gamma_K - \gamma_k}\right). \quad (2.11)$$

Then, any value of the flow variables $V(\alpha, \beta, \gamma)$, like the wind speed, inside a hexahedral element, can be interpolated from the solutions V_{IJK} , $I, J, K = 1, \ldots, N+1$, on the Legendre-Gauss-Lobatto points as follows:

$$V(\alpha, \beta, \gamma) = \sum_{I=1}^{N+1} \sum_{J=1}^{N+1} \sum_{K=1}^{N+1} L_{IJK}(\alpha, \beta, \gamma) V_{IJK}.$$
 (2.12)

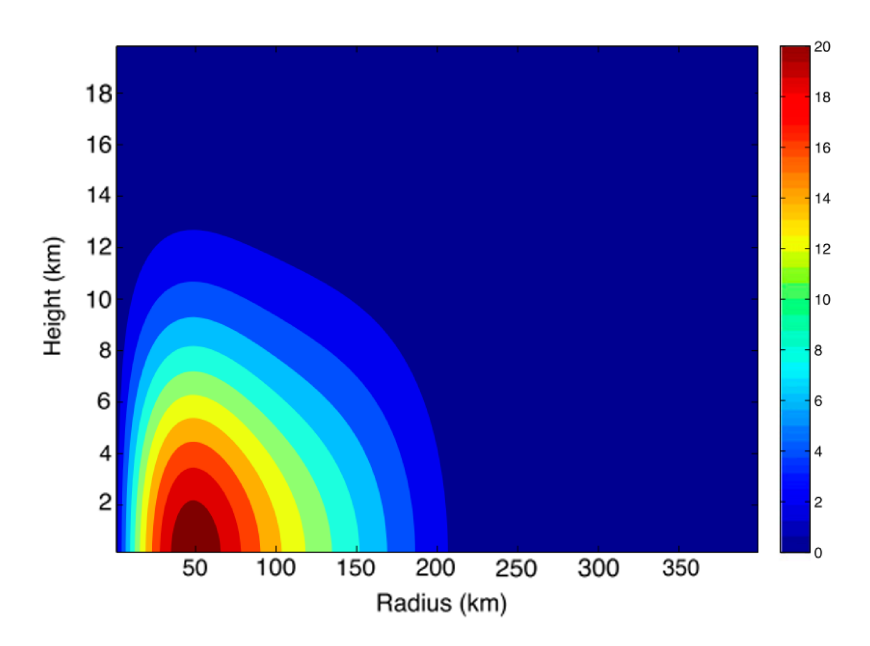


Figure 2.1: Axisymmetric tangential velocity (m/s) in the radius-height plane for the initial vortex used in each model.

Each model has identical initial conditions. In this work, we apply the ax-

isymmetric tangential winds from the tropical storm-like vortex stated in Eq. (10) of Guimond et al. [32], which is comparable to the research presented in Nolan et al. [41]. Fig. 2.1 shows this initial vortex's radius—height tangential velocity field. On top of this vortex, WRF and NUMA add four-dimensional latent heating/cooling rates derived from aerial Doppler radar observations in rapidly strengthening Hurricane Guillermo (1997). Grid spacings of 2 km horizontally and 0.5 km vertically are used to calculate these heating fields, which are then projected outward from the system's core to a radius of $\sim 60 \ km$. Each heating picture is 34 minutes long, covering $\sim 5.7 h$. The highest heating occurs at 25 to 30 km, which is well inside the original vortex's radius of maximum wind (RMW) ($\sim 50 \text{ km}$). This heating and vortex design depict the rapid intensification process driven by convective bursts [42–45]. An exhaustive uncertainty analysis by Guimond et al. [46] indicated that the latent heat retrievals were generally correct, especially for convective bursts, with randomly distributed uncertainties in the heating magnitudes of $\sim 16\%$ for updrafts higher than 5 m/s. In addition, Guimond et al. [47] used the heating retrievals in realistic forecasts of Guillermo and discovered a high degree of consistency between the predicted and observed wind fields.

The first heating field is injected into the model from the initial conditions over 30 minutes using a hyperbolic tangent function. The following heating fields are linearly interpolated over a 34-minute window to the next observation time. Our simulations stop after 6 hours of steady heating after the final observation time. A temporal evolution function is employed to regulate the forcing in the models, and Fig. 2.2 displays the three-dimensional structure of the heating for three fields. Three

fields of this heating show the storm-centered volume extending 120 km horizontally and 20 km vertically. Unless otherwise stated, the time evolution function that forces heating into the model is represented in minutes. To ensure numerical stability, we have implemented a fading exponential function at the top of the observational domain (10 km) to integrate the data into the model grid gently.

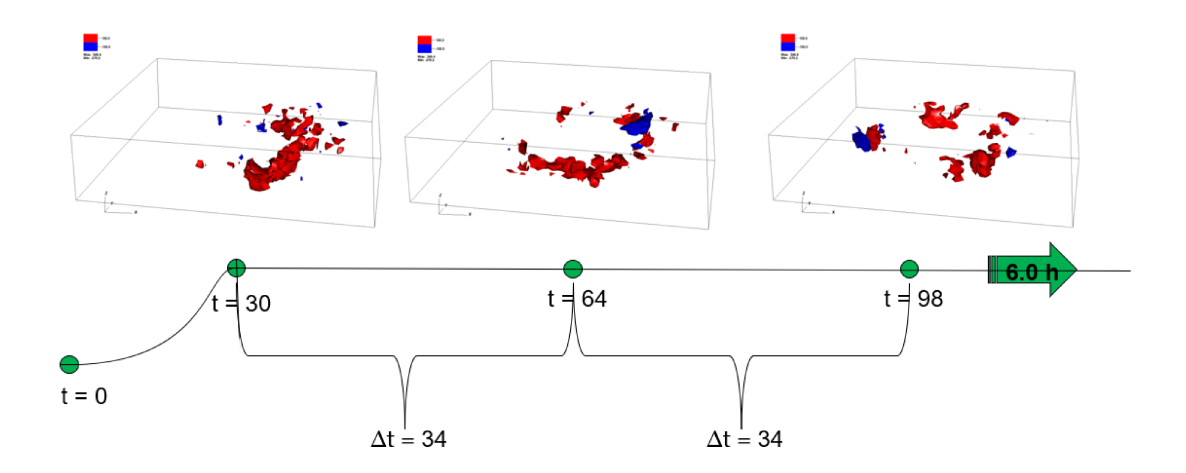


Figure 2.2: Three-dimensional iso-surfaces of latent heating (red; 100~K/h) and cooling (blue; -100~K/h) retrieved from airborne Doppler measurements in rapidly intensifying Hurricane Guillermo (1997).

The same explicit diffusion settings are also given to both models. We can compare WRF and NUMA using the same sub-grid scale turbulence scheme. However, because each model has a different dynamic core and dissipation characteristics, the eddy viscosity values will likely change as the simulations continue. Following the results of the WRF 3D turbulent kinetic energy (TKE) sub-grid turbulence scheme, we constructed a simple height-dependent eddy viscosity model to attribute model discrepancies solely to the numerical formulation. At first, we ran a WRF simula-

Table 2.1: Numerical methods, boundary conditions and sub-grid scale diffusion used in WRF and NUMA simulations.

Description	WRF	NUMA
Time Integration	Split-explicit with 3^{rd}	Semi-implicit with
	order Runge-Kutta	2^{nd} order leapfrog
Spatial Discretization	Finite difference on C	Spectral element
	grid	
Explicit Filters	None	1^{st} order temporal
Boundary Conditions	Periodic in x & y co-	Same as WRF
	ordinates, gravity wave	
	sponge on top and free-	
	slip on bottom	
Sub-grid Scale Diffusion	Height-dependent eddy	Same as WRF
	diffusion for momentum	
	and scalars based on	
	TKE	
Physics	None	Same as WRF

tion with the 3D TKE scheme to get an idea of how the vortex and heating affected the viscosity and diffusivity of the eddy. In this scheme, the sources and sinks of TKE after a parcel depend on its shear, buoyancy, and energy loss. Skamarock et al. [48] has information about how this plan was implemented in WRF, including how the dissipation parameters were set. TKE will be produced by the observed heat forcing from both the buoyancy and shear components. Still, we only look at the results of the eddy viscosities and diffusivities, which can be found using the following formulas:

$$K_{h,v} = C_k l_{h,v} \sqrt{e} \tag{2.13}$$

Where e is the TKE, C_k is a constant of 0.15, and l is a length scale of about 2000 m in the horizontal direction and 375 m in the vertical direction. Figure 2.3

shows plots of the horizontal eddy viscosity from the 3D TKE scheme at the height of 6 h and a distance of 0.50km and 9.80km, respectively. Viscosities $\sim 240~m^2s^{-1}$ or higher are seen in the figures, showing the eyewall as a narrow ring at the height of 0.5 km and a wider area $500-750~m^2s^{-1}$ at the height of 9.80 km.

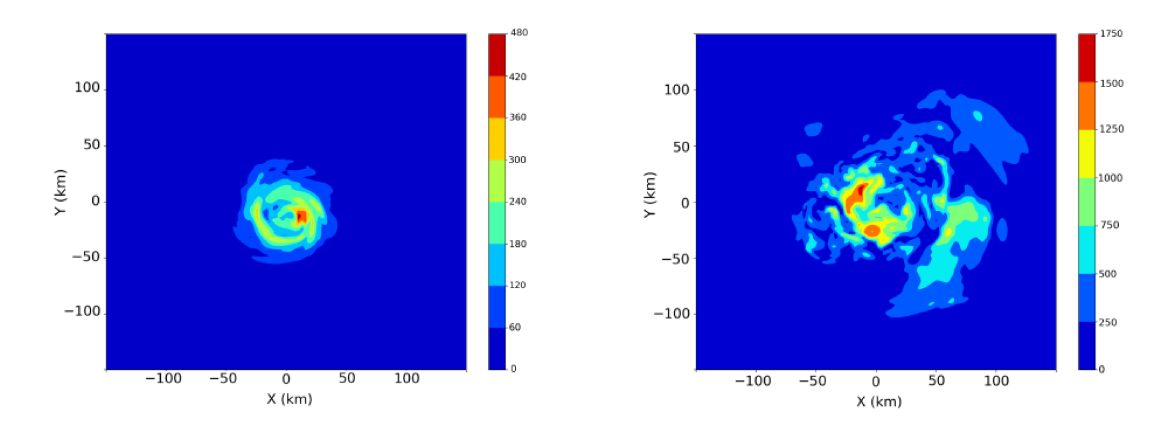


Figure 2.3: Eddy viscosity (m^2s^{-1}) values output from the WRF 3D TKE scheme at 6 h and 0.5 km height (left panel) and 9.8 km height (right panel).

Large, vertically coherent heating pulses from convective bursts are associated with localized zones with higher viscosity values of $400 \ m^2 s^{-1}$ at lower and upper levels, respectively. Remember that we have changed WRF's default value of the turbulent Prandtl number (1/3) to 1, allowing the same eddy viscosity/diffusivity values for momentum and scalars. We have taken great care to ensure that all default Prandtl number values in the WRF software are set to 1. Furthermore, NUMA has the turbulent Prandtl number set to 1. Maximum horizontal and vertical eddy viscosities generated by the 6 h WRF simulation are depicted as a function of height in Fig. 2.4. Both curves start with modest values and rise dramatically in the center, with extra oscillations to the height of $16 \ km$. Fig. 2.3 shows that the large values observed at intermediate and upper levels result from the powerful heating

pulses associated with convective bursts. The maximum values are taken over the 6 h simulation.

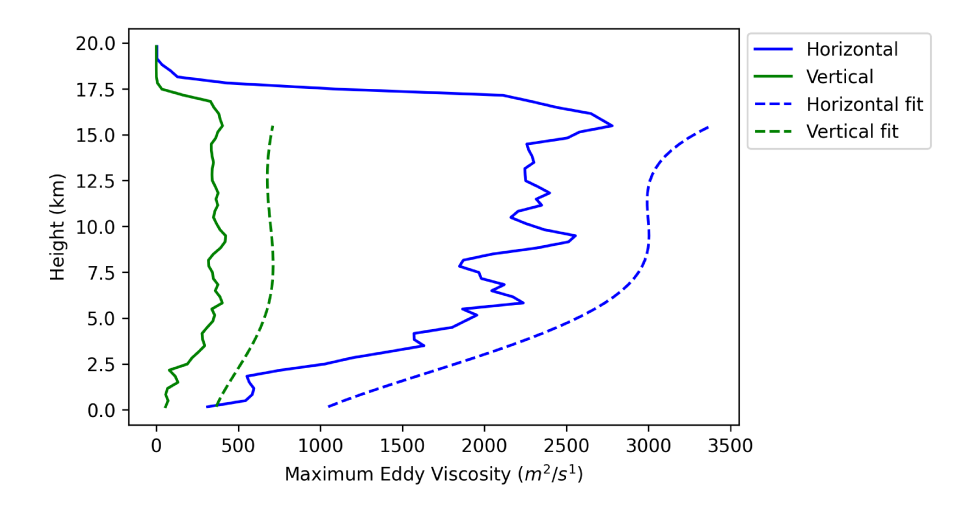


Figure 2.4: Maximum eddy viscosity values from the 3D TKE scheme in WRF as a function of height.

The maximum horizontal viscosity values are almost five times higher than their vertical counterparts. This is because the gravity wave sponge is added to the model at the height of $\sim 16~km$, after which the values rapidly decrease. The general shape and values of the eddy viscosity data are approximated by high-order polynomial fits that are superimposed on top of the maximum viscosity curves. Here is the format that these overlaps take:

$$visc(z) = \tilde{a}z^5 + \tilde{b}z^4 + \tilde{c}z^3 + \tilde{d}z^2 + \tilde{e}z + \tilde{f}$$
(2.14)

where z is the geometric height in meters and Table 2.2 shows the coefficients of the fifth-order polynomial. An additional constant was added to the \tilde{f} coefficient for both the horizontal and vertical polynomial fits. This was done so that the NUMA code would become more stable. The \tilde{f} coefficient may be found in Table 2.2, and the

curves in Fig. 2.4 take into account this offset. In the final step of the comparison simulations, the height-dependent eddy viscosity values are input into WRF and NUMA for momentum and scalar diffusion. The purpose of this straightforward explicit diffusion model is not only to stabilize each numerical model but also to depict, at least to some extent, the actual sub-grid size turbulent diffusion that results from the TKE scheme.

Table 2.2: Coefficients for the horizontal and vertical viscosity polynomial fits.

Coefficients	\tilde{a}	$ ilde{b}$	\tilde{c}	$ ilde{d}$	\tilde{e}	$ ilde{f}$
Horizontal	-0.012760	0.6946	-11.57	53.28	255.90	1003.90
Vertical	-0.004572	0.2150	-3.29	15.05	43.16	357.65

Chapter 3: Comparison of WRF & NUMA Simulations

3.1 Time Series and Structure of Windspeed

Here, we examine the differences between the WRF and NUMA control simulations concerning the structure of windspeed perturbations and the time series of horizontal wind speed and kinetic energy. In this context, "perturbation" refers to the difference between the overall wind speed at a given moment and the wind speed that existed under the beginning condition. This difference can be used to determine the wind structures that were created due to observational heating. Fig. 3.1 illustrates the control WRF and NUMA simulations' maximum windspeed output per 30 minutes. Maximum winds increased by 45 m/s in 6 h, an actual RI rate. The more powerful (and weaker) starting vortex produces a solid inward flow of angular momentum and increased winds, which accounts for the high rate. When comparing the RMW of the initial vortex utilized in this study ($\sim 50 \text{ km}$) to that used in Guimond et al. [47] ($\sim 30 \text{ km}$), it is clear that the latter is more appropriate given the more considerable amount of heating observed in the present investigation. The realistic beginning vortex lowered the minimum pressure by $12-15 \ hPa$ in $6 \ h$, which was closer to observations than the present vortex. This thesis analyzes the idealized vortex response to heating pulses obtained from observations in a RI system and examines implicit numerical dissipation. We will not replicate Guillermo.

Thus, the initial vortex and model setup is adequate for our work.

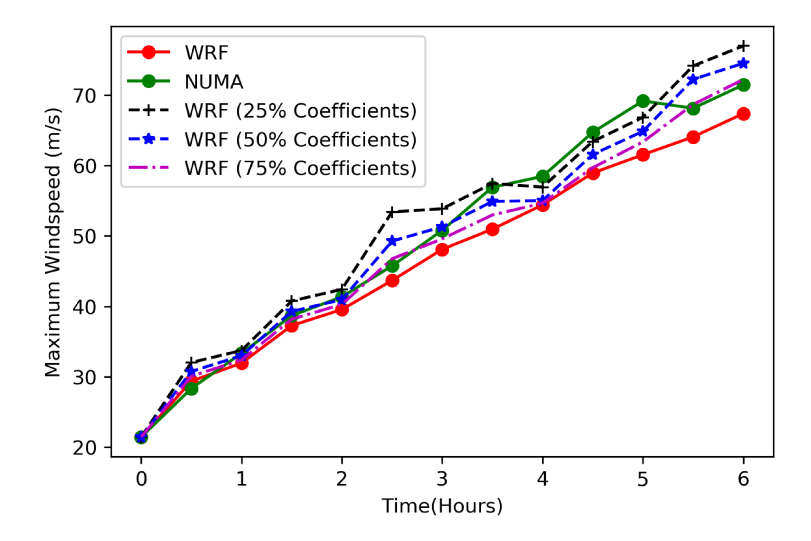


Figure 3.1: Time series of maximum windspeed for the control WRF and NUMA simulations.

After $\sim 2~h$, the NUMA winds begin to grow in comparison to WRF, and Fig. 3.1 also indicates that throughout a final couple of hours of the simulations, the maximum windspeed is 2-7 m/s or 4-12% greater in NUMA in comparison to WRF. A time series of minimum pressure perturbation was also investigated (although not presented), and the evolution was found to be quite similar to the one shown in Fig. 3.1. NUMA produced minimum pressures of 5.5 to 6.5 hPa lower than WRF during the last several hours of the simulation. Dashed lines represent sensitivity experiments performed in WRF with eddy viscosity values adjusted to a specified fraction of their default values. Three WRF sensitivity experiments were performed using eddy viscosity values of 25%, 50%, and 75% of the default values to match WRF and NUMA time series. The 75% tests indicate substantially lower maximum winds than NUMA, but the 25% tests look excessively high, especially before 3.5 h.

Despite the anomalously high value at 2.5 h, the 50% tests match NUMA better up to 3.5 h. Smoothing out the higher variability between 4 and 6 h shows an excellent match to NUMA. These results imply that WRF needs reduce explicit diffusion by 50% to generate a similar intensity time series to NUMA.

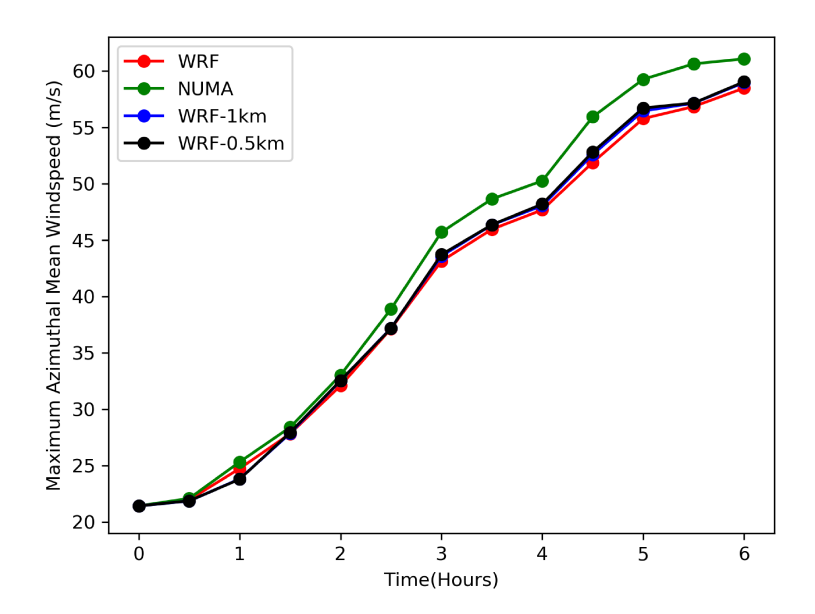


Figure 3.2: Time series of maximum azimuthal mean windspeed for the control WRF and NUMA simulations as well as higher horizontal resolution WRF simulations at 1 km and 0.5 km.

Azimuthal mean time series diagnostics were also calculated. As shown in Fig. 2.2, the observational heat forcing has an azimuthal wavenumber-one structure that steadily drives the vortex to the southeast. The storm center is calculated by iteratively maximizing azimuthal mean windspeed. The data are interpolated into a cylindrical grid centered on the storm center, and the azimuthal mean quantities are computed. Figures 3.2 and 3.3 show the time series of the maximum azimuthal mean wind speed and the mean kinetic energy, respectively. These figures demonstrate a

qualitative pattern comparable to the maximum windspeed, with NUMA providing higher azimuthal mean windspeeds and kinetic energy values than WRF, with those disparities expanding with time. In the last few hours, NUMA's highest azimuthal mean windspeed has been rough 4 m/s or 8% greater than in WRF. Since the average kinetic energy follows a trend quite similar to that of the wind speed, it can be utilized as a point of departure for the dynamical budget analysis described in Section 3.2 to shed light on the discrepancies between the models.

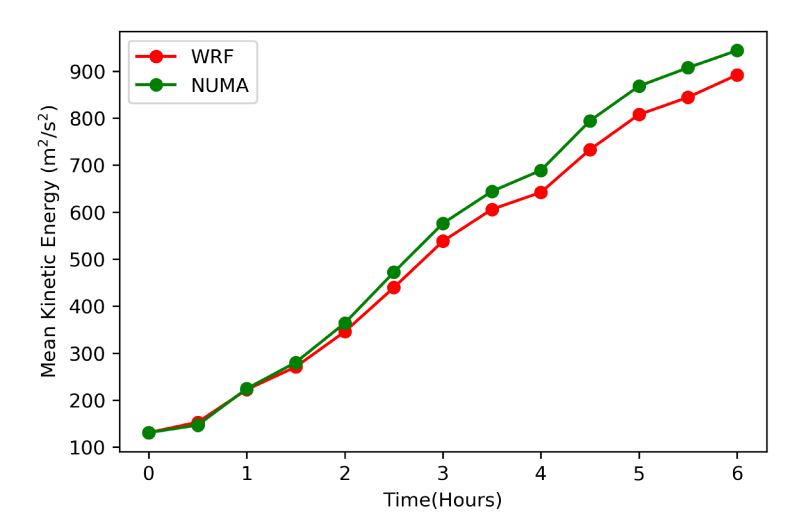


Figure 3.3: Time series of azimuthal mean kinetic energy averaged over the eyewall ($\sim 10-50~km$ radius) and height ($\sim 0.19-1.5~km$) for the control WRF and NUMA simulations.

The maximum azimuthal mean windspeed from 1 km and 0.5 km WRF simulations is also displayed in Fig. 3.2. These simulations are identical to the WRF control run except for the horizontal grid spacing, which lets one see how implicit numerical dissipation changes with a finer mesh. The WRF mean wind speed goes up between 3 and 6 hours for the 1 km and 0.5 km runs compared to the 2 km

control case, with peak differences of about 1 m/s. However, there are very few, if any, changes in the highest azimuthal mean windspeed metric between the WRF 1 km and 0.5 km simulations. These results show that increasing horizontal resolution by at least a factor of two reduces WRF's implicit numerical dissipation and creates a stronger vortex that is more like NUMA.

Section 3.2 will detail why WRF produces a lower intensity response than NUMA. We now see that while the differences between WRF and NUMA for the mean quantities given in Figs. 3.2 and 3.3 are relatively small, there is much greater variability on smaller spatial and temporal scales. Further grid modifications, particularly in the vertical (not investigated), may result in considerable increases in intensity. The idealized character of the setup and the relatively limited time duration of these simulations (determined by the available observations) will also restrict the range of possible outcomes.

The fluctuations and variations in horizontal wind speed (m/s) for 4 h for WRF and NUMA are shown in Fig. 3.5. The WRF results are displayed in panels (a) and (b) at 0.19 km and 4.83 km altitudes, while the NUMA results are shown in panels (c) and (d) at the exact altitudes. Differences between NUMA and WRF are displayed at equivalent heights in panels (e) and (f). As shown in Fig. 3.5, the vortex has reached its maximum intensity between the hours of 5 and 6 hours, with perturbation windspeeds of around 60 meters per second being recorded on the northern and northeastern sides of the storm. The RMW of the vortex is between 15 and 20 kilometers at these time intervals, with NUMA on the lower side of that interval and WRF on the higher side of that interval. The RMW of the first vortex

was about 50 km, and the fast rate at which it shrunk is consistent with the fact that the winds were picking up speed quickly.

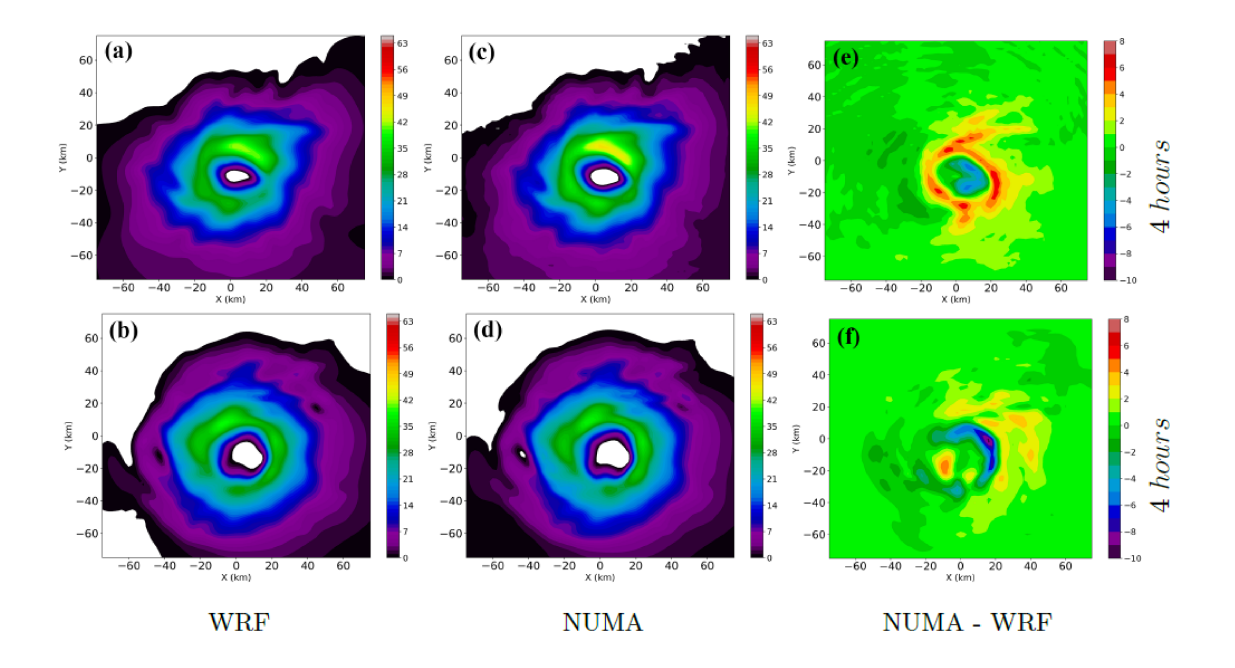


Figure 3.4: Horizontal wind speed perturbations (m/s) and differences (m/s) at 4 h for WRF and NUMA at 0.19 km and 4.83 km height levels. Panels (e) and (f) show the differences (NUMA - WRF) at the same corresponding height levels.

NUMA's low-wind eye is broader than WRF's, much as in the previous period. Winds within an important area of the northern eyewall are 7-8 m/s stronger in NUMA than in WRF at 5 h, with peak differences as high as +12 m/s. This leads to significant little variances between the two and a more pronounced radial wind gradient. North and northeast of the storm, you can make out some narrow zones of more substantial wind differences, which may be connected to the dynamics of the vortex Rossby waves. Even if the local wind differences are smaller at 6 h, they

are still substantial because much of the eyewall has positive differences of about 5 m/s, with more significant values on the Eastern side of the vortex.

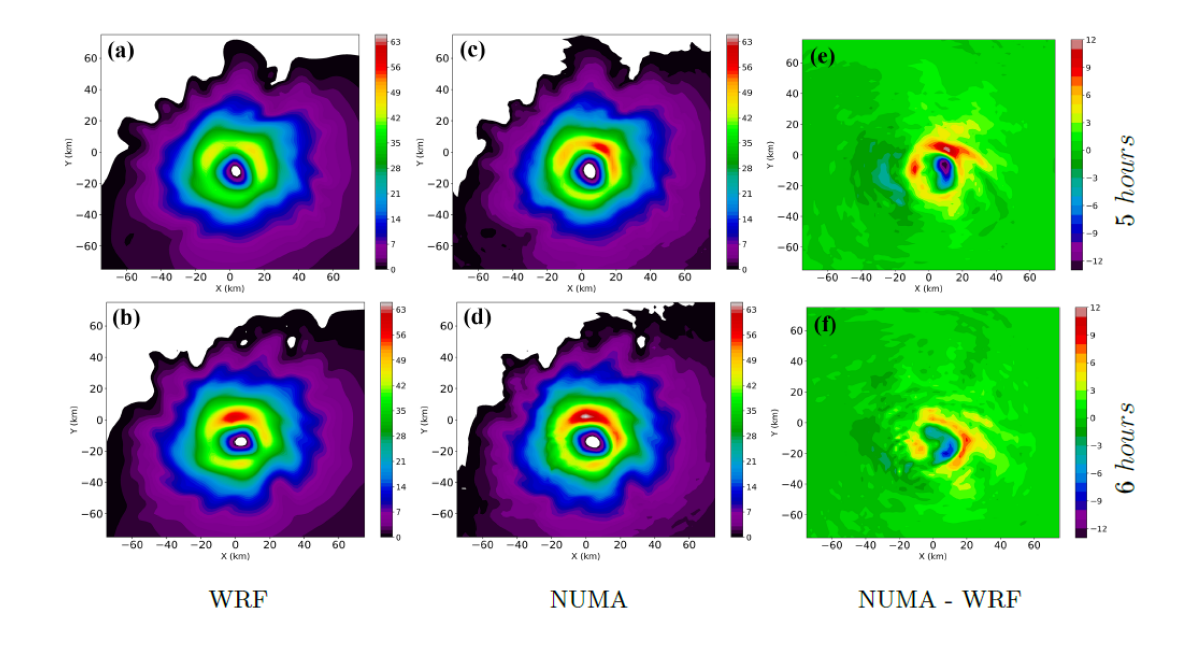


Figure 3.5: The same as in Fig. 3.4, only showing the 0.19 km height level at 5 h and 6 h in WRF in panels (a) and (b), respectively and NUMA in panels (c) and (d). Panels (e) and (f) show the differences (NUMA - WRF) at the same corresponding time periods.

Wind speed differences (NUMA - WRF) at 0.19 km height at 4 h, 5 h, and 6 h as a function of WRF grid spacing are depicted in Fig. 3.6. For convenience, the differences at 2 km WRF spacing are presented again in the first row of Fig. 3.6. If we look at Fig. 3.6, we can see that decreasing the grid spacing from 2 km to 1 km in WRF decreases the differences with NUMA and generates a stronger vortex in the eyewall region by 2 - 3 m/s across the board. The largest shifts are found in specific areas, like the eye and the northern eyewall in Figs. 3.6b and Figs. 3.6e,

respectively. Wind speed variations are reduced by only a negligible about $0.5 \ m/s$ when switching from $1 \ km$ to $0.5 \ km$ in WRF simulations. The maximum azimuthal mean windspeed measure depicted in Fig. 3.2 agrees with these findings.

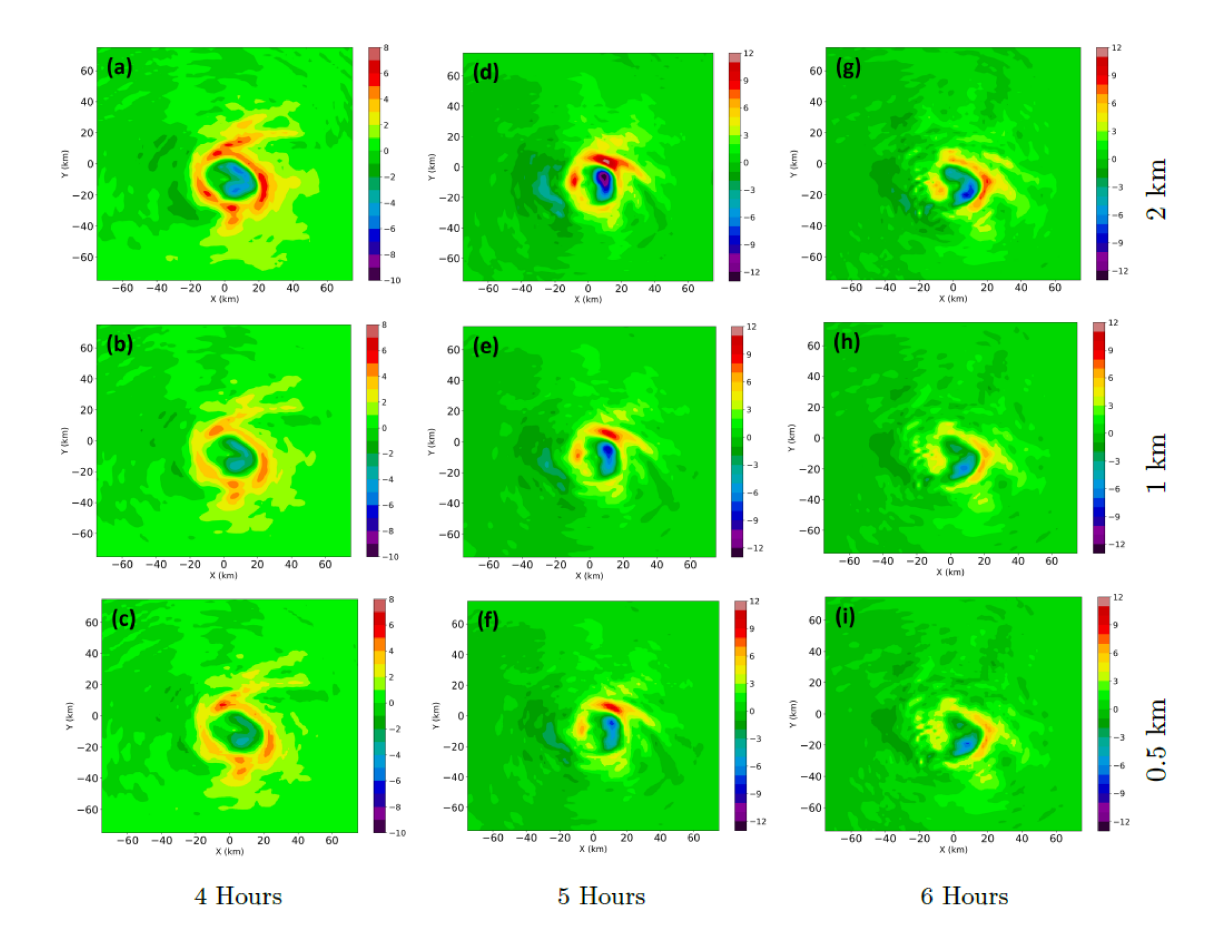


Figure 3.6: Horizontal wind speed differences (NUMA - WRF) in (m/s) at 0.19 km height at 4 h, 5 h and 6 h for the control NUMA simulation and varying horizontal grid spacing in WRF (2 km, 1 km and 0.5 km). Each panel is identified according to the row (WRF resolution) and column (time period) as denoted on the figure.

3.2 Budget Analyses

The last section demonstrated substantial distinctions between the two numerical models, with NUMA providing a more pronounced intensity response. Given that every model was set up in the same way, with the same initial circumstances and heat forcing, how is this even possible? The answer to this question lies in the structure of the numerical methods that form the models' respective dynamical cores. In this section, we study how the intensity differences are created and emphasize areas of the numerical scheme driving this impact.

In cylindrical coordinates, the horizontal kinetic energy of the azimuthal mean vortex (r, θ, z) is expressed as

$$\bar{K} = \frac{1}{2}(\bar{u}^2 + \bar{v}^2) \tag{3.1}$$

Here u represents the radial windspeed, v represents the tangential wind speed, and the overbar represents an azimuthal mean quantity. These variables and those that follow are functions of the radius (r) and height (z) after an azimuthal average has been performed. The transport equation for azimuthal mean kinetic energy can be found by multiplying the radial and tangential equations of motion by their corresponding velocities, summing the two equations, and then applying Reynolds decomposition in the azimuthal direction. The over bar and prime notations below show the azimuthal mean and eddy variables. Beginning with the radial and tangential equations of motion on an f-plane and considering the anelastic approximation

 $\rho = \bar{\rho}(z)$:

$$\frac{Du}{Dt} - \frac{v^2}{r} - f_o v = -\frac{1}{\bar{\rho}} \frac{\partial \hat{p}}{\partial r} + D_r \tag{3.2}$$

$$\frac{Dv}{Dt} + \frac{uv}{r} + f_o u = -\frac{1}{\bar{\rho}r} \frac{\partial \hat{p}}{\partial \theta} + D_{\theta}$$
(3.3)

The total derivative in cylindrical coordinates is:

$$\frac{D}{Dt} = \frac{\partial}{\partial t} + u \frac{\partial}{\partial r} + \frac{v}{r} \frac{\partial}{\partial \theta} + w \frac{\partial}{\partial z}$$

Breaking Eqs. (3.2) and (3.3) into mean and turbulent parts, azimuthally averaging and transforming the resulting equations into flux form:

$$\frac{\partial \bar{u}}{\partial t} + \frac{1}{r} \frac{\partial \bar{u} \bar{u} r}{\partial r} + \frac{1}{r} \frac{\partial \bar{u}' u' r}{\partial r} + \frac{1}{\bar{\rho}} \frac{\partial \bar{u} \bar{w} \bar{\rho}}{\partial z} + \frac{1}{\bar{\rho}} \frac{\partial \bar{u}' w' \bar{\rho}}{\partial z} - \frac{\bar{v} \bar{v}}{r} - \frac{\bar{v}' v'}{r} - f_o \bar{v} = -\frac{1}{\bar{\rho}} \frac{\partial \bar{p}}{\partial r} + \overline{D_r}$$

$$(3.4)$$

$$\frac{\partial \bar{v}}{\partial t} + \frac{1}{r} \frac{\partial \bar{u}\bar{v}r}{\partial r} + \frac{1}{r} \frac{\partial \overline{u'v'}r}{\partial r} + \frac{1}{\bar{\rho}} \frac{\partial \bar{v}\bar{w}\bar{\rho}}{\partial z} + \frac{1}{\bar{\rho}} \frac{\partial \overline{v'w'}\bar{\rho}}{\partial z} + \frac{\bar{u}\bar{v}}{r} + \frac{\bar{u}'\bar{v}'}{r} + f_o\bar{u} = \overline{D_{\theta}}$$
 (3.5)

Using the definition of kinetic energy, we multiply \bar{u} with Eq. (3.4) and \bar{v} with Eq. (3.5) and recognizing the relation $\bar{u}\frac{\partial \bar{u}}{\partial t} = \frac{\partial}{\partial t}(\frac{\bar{u}^2}{2})$ for the radial equation, for example, we find:

$$\frac{\partial}{\partial t}(\frac{\bar{u}^2}{2}) + \frac{1}{r}\frac{\partial(\frac{\bar{u}^2}{2}\bar{u}r)}{\partial r} + \frac{\bar{u}}{r}\frac{\partial \bar{u}'\bar{u}'r}{\partial r} + \frac{1}{\bar{\rho}}\frac{\partial(\frac{\bar{u}^2}{2}\bar{w}\bar{\rho})}{\partial z} + \frac{\bar{u}}{\bar{\rho}}\frac{\partial \bar{u}'\bar{w}'\bar{\rho}}{\partial z} - \frac{\bar{u}\bar{v}\bar{v}}{r} - \frac{\bar{u}\bar{v}'\bar{v}'}{r} \\
-f_o\bar{u}\bar{v} = -\frac{\bar{u}}{\bar{\rho}}\frac{\partial\bar{p}}{\partial r} + \bar{u}\overline{D_r}$$
(3.6)

$$\frac{\partial}{\partial t} \left(\frac{\bar{v}^2}{2} \right) + \frac{1}{r} \frac{\partial \left(\frac{\bar{v}^2}{2} \bar{u}r \right)}{\partial r} + \frac{\bar{v}}{r} \frac{\partial \bar{u}' \bar{v}' r}{\partial r} + \frac{1}{\bar{\rho}} \frac{\partial \left(\frac{\bar{v}^2}{2} \bar{w} \bar{\rho} \right)}{\partial z} + \frac{\bar{v}}{\bar{\rho}} \frac{\partial \bar{v}' \bar{w}' \bar{\rho}}{\partial z} + \frac{\bar{u} \bar{v} \bar{v}}{r} + \frac{\bar{v} \bar{u}' \bar{v}'}{r} + \frac{\bar{v} \bar{u}' \bar{v}'}{r} + \frac{\bar{v} \bar{u}' \bar{v}'}{r} + \frac{\bar{v} \bar{u}' \bar{v}' \bar{v}' \bar{v}'}{r} + \frac{\bar{v} \bar{u}' \bar{v}' \bar{v}' \bar{v}'}{r} + \frac{\bar{v} \bar{u}' \bar{v}' \bar{v$$

By adding Eq. (3.6) and Eq. (3.7) and again recognizing the definition of kinetic energy, we arrive at Eq. (3.9), which is the transport equation for azimuthal mean kinetic energy,

$$\frac{\partial \bar{K}}{\partial t} = -\frac{1}{r} \frac{\partial}{\partial r} (\bar{u}\bar{K}r) - \frac{1}{\bar{\rho}} \frac{\partial}{\partial z} (\bar{w}\bar{K}\bar{\rho}) - \frac{\bar{u}}{r} \frac{\partial}{\partial r} (\bar{u}'\bar{u}'r) - \frac{\bar{u}}{\bar{\rho}} \frac{\partial}{\partial z} (\bar{u}'\bar{w}'\bar{\rho})
- \frac{\bar{v}}{\bar{\rho}} \frac{\partial}{\partial z} (\bar{v}'\bar{w}'\bar{\rho}) - \frac{\bar{v}}{r} \frac{\partial}{\partial r} (\bar{u}'\bar{v}'r) + \frac{\bar{u}\bar{v}'\bar{v}'}{r} - \frac{\bar{v}\bar{u}'\bar{v}'}{r} - \frac{\bar{u}}{\bar{\rho}} \frac{\partial \bar{\hat{\rho}}}{\partial r} + \bar{u}\bar{D}_r + \bar{v}\bar{D}_{\theta}$$
(3.8)

$$\frac{\partial \bar{K}}{\partial t} = M + E + P + D \tag{3.9}$$

where,

$$M = -\left(\frac{1}{r}\frac{\partial}{\partial r}(\bar{u}\bar{K}r) + \frac{1}{\bar{\rho}}\frac{\partial}{\partial z}(\bar{w}\bar{K}\bar{\rho})\right),$$

$$E = -\left(\frac{\bar{u}}{r}\frac{\partial}{\partial r}(\bar{u}'\bar{u}'r) + \frac{\bar{u}}{\bar{\rho}}\frac{\partial}{\partial z}(\bar{u}'\bar{w}'\bar{\rho}) + \frac{\bar{v}}{\bar{\rho}}\frac{\partial}{\partial z}(\bar{v}'\bar{w}'\bar{\rho}) + \frac{\bar{v}}{r}\frac{\partial}{\partial r}(\bar{u}'\bar{v}'r) - \frac{\bar{u}\bar{v}'\bar{v}'}{r} + \frac{\bar{v}\bar{u}'\bar{v}'}{r}\right),$$

$$P = -\frac{\bar{u}}{\bar{\rho}}\left(\frac{\partial\bar{p}}{\partial r}\right), \quad \text{and} \quad D = \left(\bar{u}\bar{D}_r + \bar{v}\bar{D}_\theta\right).$$

M denotes the mean kinetic energy transport terms, E denotes the eddy trans-

port terms representing the Reynolds stress contributions in the azimuthal dimension, P denotes the pressure gradient term, and D is the total explicit diffusion term in Eq. (3.9). After averaging the fields over the eyewall (10 – 50 km radius) and height (0.19 - 1.5 km), a time series of azimuthal mean kinetic energy budget tendencies are shown in Fig 3.7. The most important term, the pressure gradient, increases the vortex's mean kinetic energy, as seen in Fig. 3.3. Input heating increases integrated warming in the storm center and the radial pressure gradient between the undisturbed outlying regions and reduces pressures in the core region. This higher radial pressure differential produces significant low-level inflow, which conveys high angular momentum from the storm's outer areas to the center, boosting the vortex's tangential velocity. NUMA outperforms WRF in the pressure gradient term, notably beyond 2 h, by 25–40%.

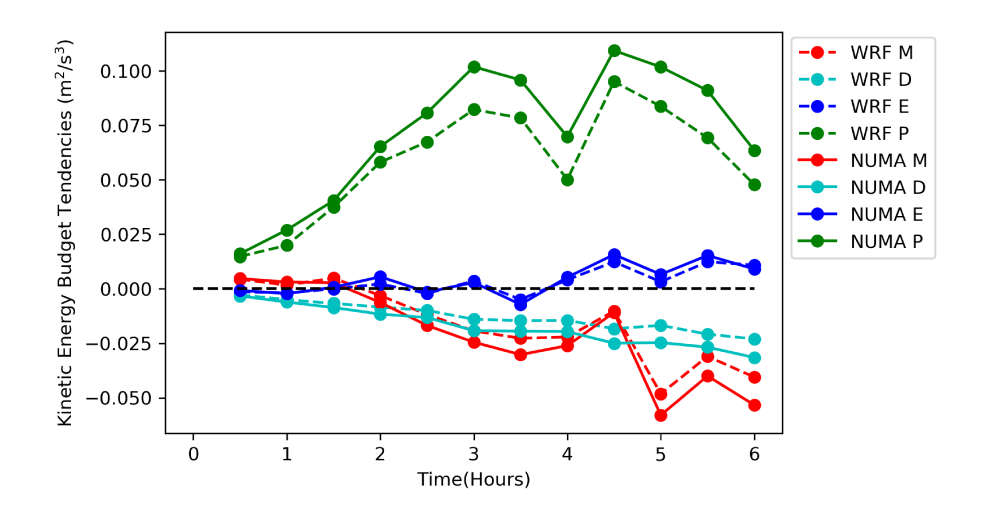


Figure 3.7: Time series of azimuthal mean kinetic energy budget tendencies from both models after averaging.

As the mean flow intensifies, the mean transport term contributes to the second

most. The heating profile is highest near middle levels; therefore, mean vertical transport outweighs horizontal transport. Thus, the lower levels of the vortex have a considerable positive flux of kinetic energy, resulting in a net energy sink. The mean transfer term is about 4.5 times smaller than the pressure gradient in WRF and NUMA. After 3.5 h, the eddy transport term contributes positively to mean kinetic energy. After adding all budget factors, eddy transport increases the vortex's mean KE by 15–40% over 6 h. Eddy transport (E in Eq. (3.9)) adds 18% to mean kinetic energy when integrating budget terms over time. We find that the mean kinetic energy in our analysis domain has a positive trend toward these latter times when the vertical divergence of the vertical tangential momentum flux reaches its most significant values. The dashed black line indicates zero tendencies in Fig 3.7.

The total explicit diffusion term values are similar before 1 h. However, after that time, the values from NUMA begin to gradually increase relative to WRF, which results in significant differences later during the simulation (NUMA is larger than WRF by 36% when averaged from 2 to 6 h). The reason for this is that even though the values of the eddy viscosity are constant, the velocity gradients in NUMA are more prominent than those in WRF (as was discussed in part before this one), which results in a greater magnitude in the Laplacian operator. This is not an accurate representation of how each code's implicit numerical dissipation compares. A straightforward diagnostic calculation that considers this influence is presented in the following paragraphs. The total explicit diffusion term values are similar before 1 h. However, after that time, the values from NUMA begin to gradually increase relative to WRF, which results in significant differences later

during the simulation (NUMA is larger than WRF by 36% when averaged from 2 to 6h). Even though the values of eddy viscosity are constant, velocity gradients in NUMA are more prominent than those in WRF (as was discussed in part before this one), which results in a greater magnitude in the Laplacian operator. This is not an accurate representation of how each code's implicit numerical dissipation compares. A straightforward diagnostic calculation that considers this influence is presented in the following paragraphs.

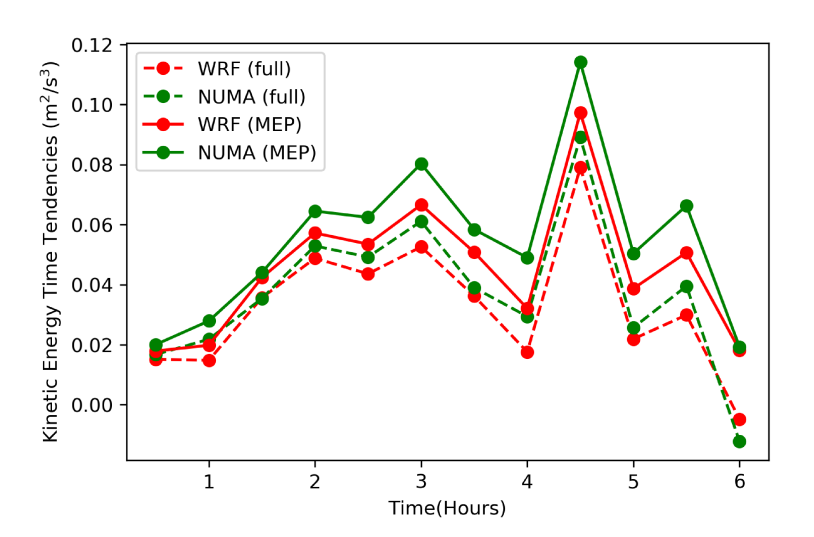


Figure 3.8: Time series of the summation of terms that control the time tendency of azimuthal mean kinetic energy on the RHS of Eqn (3.9). The dashed lines represent all terms on the RHS of Eq. (3.9), while the solid lines include only the M, E and P terms. After summation, the fields are averaged as is done in Fig. 3.7.

The time series of the sum of all terms on the right-hand side of Eq. (3.9) for WRF and NUMA is shown in Fig. 3.8. Fig. 3.3 shows the slope of the curves in the time series of mean kinetic energy. The simulation intensifies except for the last

output time at 6 h, which is why Fig. 3.3 does not reflect this weakening. Except for a massive spike at 4.5 h, the intensification rate is 0.03–0.05 m^2/s^3 throughout the simulation. NUMA has a more significant mean (azimuthal mean and averaged over $r = 10 - 50 \ km$ and $z = 0.19 - 1.5 \ km$) kinetic energy than WRF by $\sim 8\%$. This discrepancy needs to account for NUMA's increased explicit diffusion, which makes it challenging to identify implicit numerical dissipation. To remedy this, we recalculated the integrated mean kinetic energy without the explicit diffusion term (D) and found that NUMA is 18% higher than WRF. Despite the efforts to fit curves to the TKE output, we see the explicit diffusion term as a stabilizer of the numerical schemes and, to some degree, as part of the sub-grid physics (turbulence), which is unsophisticated in this context. Sub-grid physics will be investigated further in future research. Of course, there is no secure way to disentangle the effects of implicit numerical dissipation without explicit diffusion via offline integration. Due to the coupled, nonlinear evolution of the fields, differences in the explicit diffusion influence other variables in the mean kinetic energy during simulations. Since this is hard to regulate, we will not be touching on it more. Despite the efforts to fit curves to the TKE output, we see the explicit diffusion term as a stabilizer of the numerical schemes and, to some degree, as part of the sub-grid physics (turbulence), which is unsophisticated in this context. Sub-grid physics will be investigated further in future research. Of course, there is no secure way to disentangle the effects of implicit numerical dissipation without explicit diffusion via offline integration. Due to the coupled, nonlinear evolution of the fields, differences in the explicit diffusion influence other variables in the mean kinetic energy during simulations. Since this

is hard to regulate, we will not be touching on it more.

Figure 3.7 shows significant model discrepancies in the pressure gradient's contribution to the mean kinetic energy, making it necessary to investigate the entire structure of this term in search of potential regional signals. In cylindrical coordinates, the components of the horizontal pressure gradient contribution to kinetic energy are given as

$$\frac{-u}{\rho} \frac{\partial \hat{p}}{\partial r}$$
 and $\frac{-v}{\rho r} \frac{\partial \hat{p}}{\partial \theta}$

Here u and v denote the radial and tangential wind speeds. The horizontal cross sections of these terms are shown in Figs. 3.9 and 3.10, averaged over low-levels $(0.19 - 1.5 \ km)$, at 4 h and 5 h into the simulations, respectively. Furthermore, select height-averaged (over the entire column) heating contributions to the models preceding these periods are presented in Figs. 3.9 and 3.10.

The heating inputs at 3.33 h and 4 h are shown in Figs. 3.9a, 3.9b. The model results favor the 4 h heating, although the heating from earlier times remains. WRF and NUMA's radial pressure term indicates an azimuthal wavenumber-2 structure in the eyewall area, coupled to the input heating structure most closely at 4 h. Localized zones of substantial positive and negative heating rates (note the feature to the west of the storm center in Fig. 3.9b) are connected with the positive/negative couplet in the radial pressure term in a similar region. The heating input and radial pressure term are misaligned due to the vortex drift to the South-East. NUMA has higher radial pressure terms than WRF, especially in localized positive zones. This

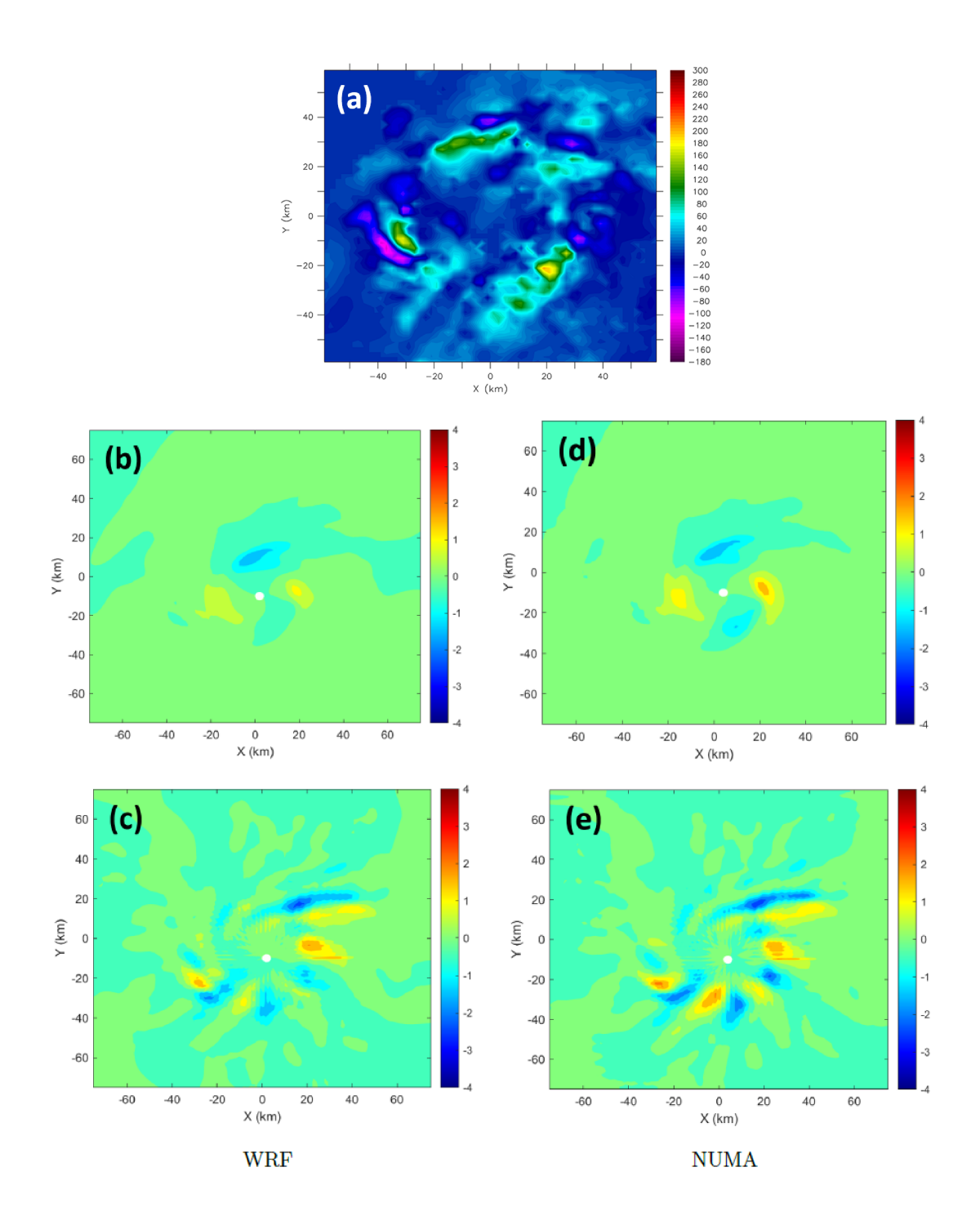


Figure 3.9: Panel (a) shows height-averaged, observational heating inputs to models around 4 h. Panels (b) and (c) demonstrate WRF's radial and tangential horizontal pressure gradient contributions (m^2s^{-3}) to kinetic energy. Panels (d) and (e) are NUMA versions of (b) and (c). Panels (b)–(e) are 4 h into the simulations.

is why the azimuthal average of these fields (Fig. 3.7) reveals NUMA with substantially bigger values than WRF. This result implies that significant, localized heating zones associated with convective bursts are causing a simultaneous, heightened pressure gradient response in NUMA that drives vortex intensification differences. Diffusion from the low-order spatial discretization of this term reduces the localized pressure gradient values in WRF.

Both WRF (Fig. 3.9d) and NUMA (Fig. 3.9f) display a distinct azimuthal wave structure with an average wavelength of sim 20 km and close to the wavenumber-5 form over this period. These waves are not examined in depth, although it is highly likely that they are convectively forced vortex Rossby waves, according to Montgomery et al. [49]. This is most easily observed to the south of the vortex center, where the Rossby waves from the projected vortex in NUMA have a bigger amplitude than those predicted by WRF. It is essential to note that minuscule oscillations in the azimuthal component of the pressure term can be observed in both the WRF and NUMA fields. These oscillations are most likely grid-scale noise in the models, although further investigation is required to prove this idea. It is more plausible that gravity waves cause these oscillations. The fields in Fig. 3.10 hours PGF are identical to those in Fig. 3.9, but they are shown 5 h into the simulations. There is a correlation between the heating snapshots at this time (Figs. 3.10a and 3.10b) and the results seen at 4 h, including localized positive anomalies in the radial pressure term with higher magnitude in NUMA than in WRF (Fig. 3.9c). The azimuthal pressure term also shows vortex Rossby waves with greater amplitude features north and east of the vortex center. At 5 h, the majority of the heating is on the east side

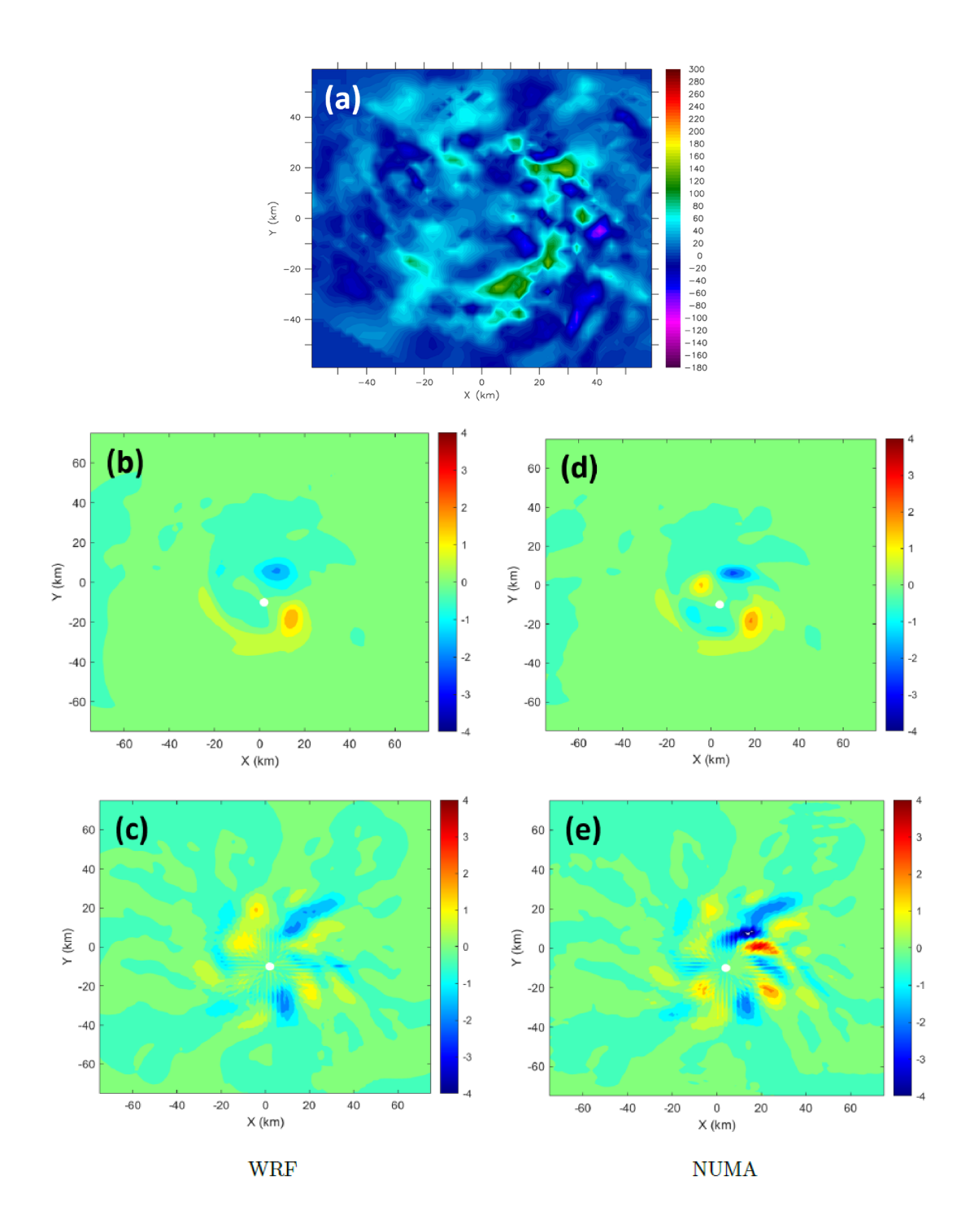


Figure 3.10: Panel (a) show the height-averaged, observational heating inputs to the models for time period $\sim 5.0~h$. All other panels are the same as in Figure 3.9, only for 5 h into the simulations.

of the vortex, with large, localized patches to the north-east of the center (Fig. 3.10b), which is in line with the greater amplitude waves in NUMA.

3.3 Longer-term Simulations Comparisons

Sections 3.1 and 3.2 compared WRF and NUMA simulations of the vortex response to 4-D observational heating administered during a brief 6h period. The specialized observations used to compute latent heating rates determined the 6h period for these simulations. Here we apply these results to 18 hours simulations by including idealized heating for the first 12 hours and then including the 6h observational heating.

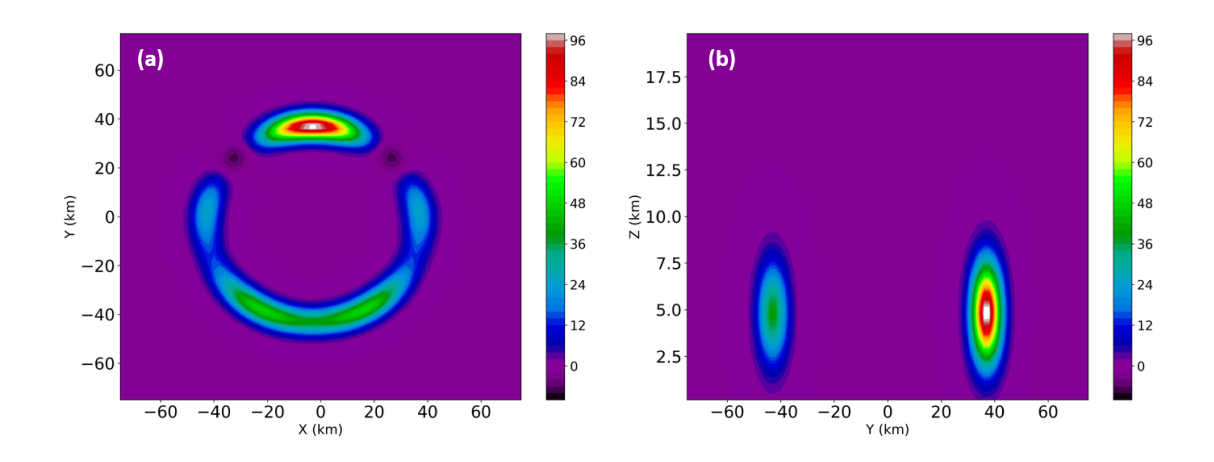


Figure 3.11: 18-h simulations' idealized heating perturbations (K/h). Panels (a) and (b) depict horizontal and vertical cross sections at z=5 km and x=0 km, respectively.

Summation of possible temperature perturbations from azimuthal wavenumbers (0, 2, 3, 4 and 5) with amplitudes of (2.0 K, 1.5 K, 1.0 K, and 1.0 K) yields

idealized heating. Because of cross-vortex flow, a wavenumber-one disturbance is not included. The peak heating rate of 100~K/h is obtained by scaling the values by the maximum and multiplying by 100. The idealized heating is focused at 5 km height and 40 km radius, directly inside the initial vortex RMW ($\sim 50~km$). A horizontal and vertical cross-section of idealized heating shows an isolated convective cell in the Northern eyewall (Fig. 3.11a) and a ring-like structure in other places with embedded asymmetries. This heating arrangement and its vertical properties (Fig. 3.11b) approximate early RI process heating [50,51]. Both models boost idealized heating to maximum capacity over 30 minutes and hold it constant for 12 h. After that, the 6 h observational heating is administered as in prior trials to simulate 18 h. This test uses WRF and NUMA control setups.

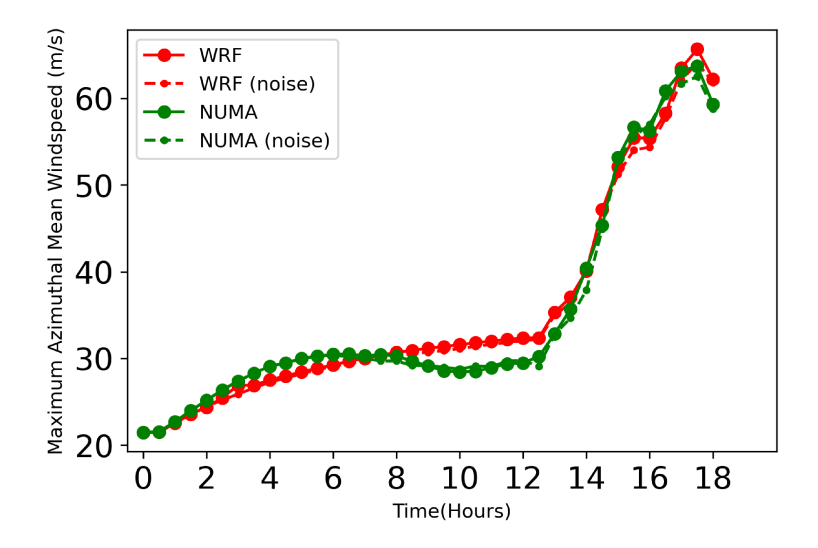


Figure 3.12: Time series of maximum azimuthal mean windspeed for the 18 hour WRF and NUMA simulations.

Maximum azimuthal mean windspeed was plotted as a time series in WRF and NUMA over the 18-hour simulation, with results shown every half an hour.

About 2 hours into the simulation, the implicit numerical diffusion effect identified in Section 3.2 causes the windspeed in NUMA to increase by 1.5 m/s relative to WRF.

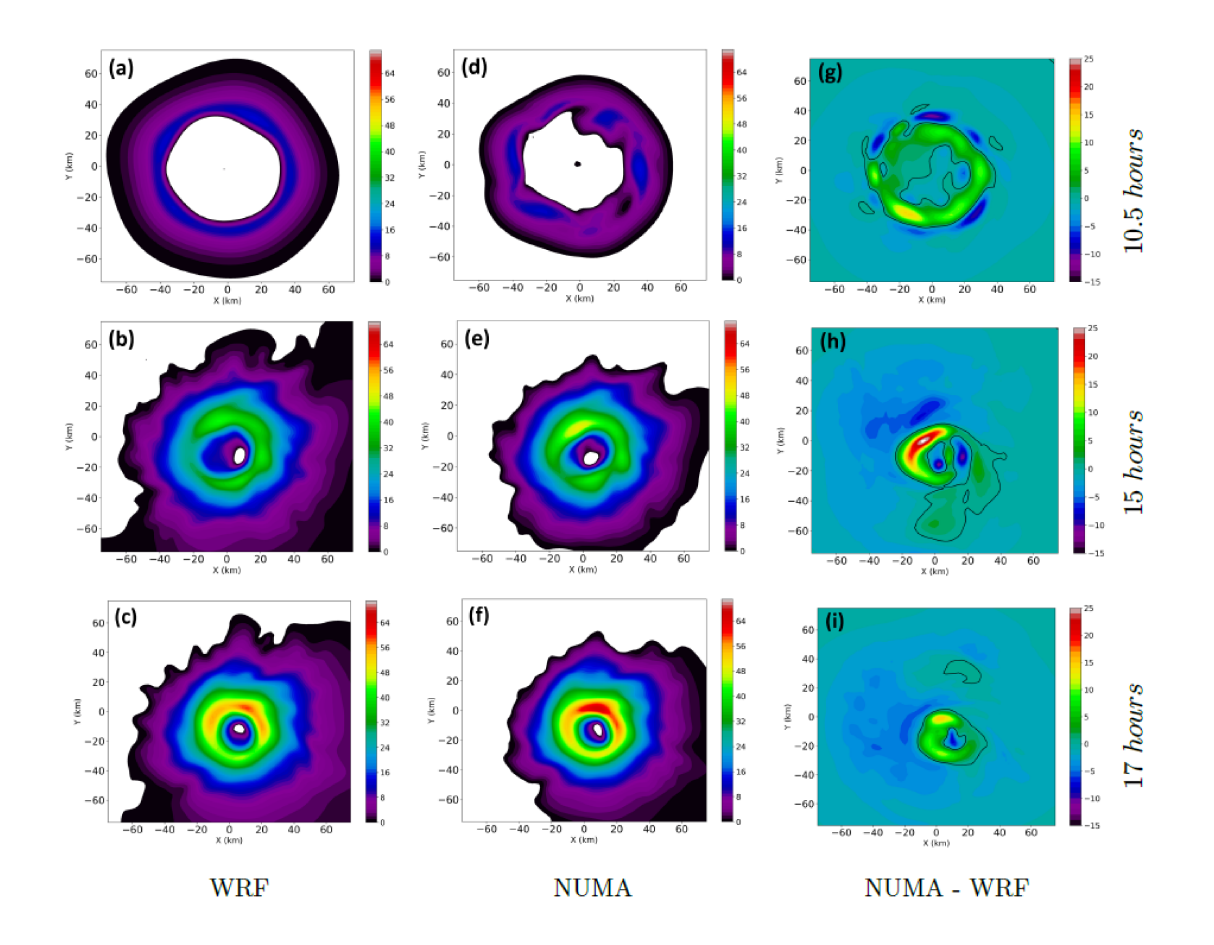


Figure 3.13: Horizontal wind speed perturbations (m/s) in each model and differences (NUMA - WRF) in (m/s) at 0.19 km height for the 18-hour simulations at 10.5 h, 15 h, and 17 h.

Between 8.0 and 14.0 hours, the windspeed in NUMA becomes noticeably lower than WRF by as much as $3.25 \ m/s$ at around 10 hours. The horizontal cross sections of windspeed perturbations at 10.5 hours and 0.19 km in height are shown in panels a, d, and g, respectively, for WRF, NUMA, and the differences (NUMA)

- WRF) in Fig. 3.13. WRF wind speed has limited azimuthal fluctuation and a reasonably consistent structure when fields are generated. At this time, the NUMA fields have high azimuthal instability due to momentum mixing between the eye and eyewall caused by heating-induced meso-vortices. As shown in Fig. 3.12, the difference plot strongly indicates momentum mixing because NUMA has greater windspeed values in the eye and lower values in the eyewall, resulting in a weaker maximum azimuthal mean windspeed.

Over time, the assumed heating perturbation produces an intense enough wave number 4 and 5 circulations to allow mixing between the vortex's eye and eyewall. WRF does not have these mixing phenomena because the implicit numerical dissipation dampens out the circulation asymmetries in the pressure gradient discretization. Therefore, in addition to significant quantitative disparities, there is also the possibility that the simulations will reveal qualitative differences at times. The mixing that NUMA produces provides a more truthful portrayal of the complexities of this arrangement. Going back to Fig. 3.12, the differences between WRF and NUMA are not as significant after 14 h. The mixing technique reduced the NUMA vortex mean intensity. The maximum azimuthal mean windspeed statistic may not necessarily indicate complete vortex intensity. Figure 3.13 illustrates the WRF and NUMA windspeed perturbations and associated difference fields for 15 and 17 hours. NUMA panels reveal greater windspeeds than WRF in the Northern and Western eyewall at 15 h and 17 h, with a massive swath of 20 m/s differences at 15 h and 10 m/s at 17 h. Operational forecasters would be concerned about these huge variances (under-predicted intensity from WRF), but Fig. 3.12 does not show NUMA's intense eyewall regions. Due to NUMA's more compact wind field, it is also essential to observe the moderate reductions in NUMA windspeed relative to WRF, radially outward of the eyewall (-5 to -8 m/s) for both 15 h and 17 h.

We also ran simulations with WRF and NUMA that included noise in the beginning conditions, in addition to the control 18-hour simulations shown in Fig. 3.12. Random perturbations within the range of $+/-0.5 \, m/s$ were incorporated into each model's initial zonal and meridional wind fields. These perturbations were applied to a ring centered on the RMW and below a height of $2 \, km$. The purpose of these noise simulations is to reflect uncertainty in the initial conditions, which will encourage nonlinear interactions and the possibility of large-scale random error at later times (also known as "chaos"). When looking at the maximum azimuthal mean wind speed intensity metric, the WRF and NUMA noise simulations demonstrate that it is very little to no difference between them at any given time. This suggests that the implicit numerical diffusion signal is substantially more significant than the noise for periods occurring before 13 hours. At the very least, this is the case before 13 hours. Given the significant asymmetric wind speed changes seen in Fig. 3.13, it is necessary to do additional research to investigate the consequences after 13 hours.

A time history of the most significant azimuthal windspeed differences for the 18 h simulations is shown in fig. 3.14. For explanation, we determined the azimuthal mean windspeed at each output time as a function of radius and height for each model run (NUMA, WRF, NUMAnoise, and WRFnoise). We then subtracted the same quantity for other combinations as indicated in Fig. 3.14. The most significant value is then reported when the difference is calculated. A time series plot of the

difference fields illustrated in Fig. 3.13g, h, and i can be appropriately characterized by following this technique.

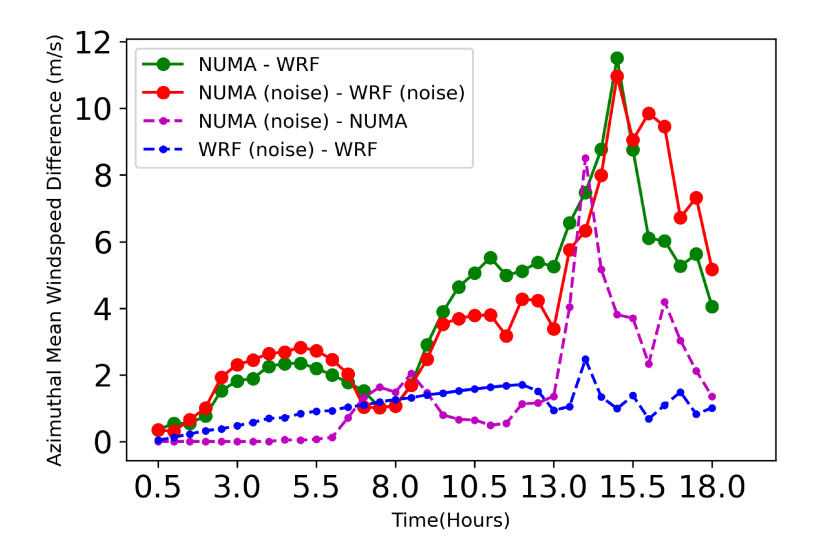


Figure 3.14: Time series of maximum azimuthal windspeed difference for the 18 hours WRF and NUMA simulations.

This bigger overall vortex intensity response from NUMA can be seen in the control simulation (NUMA - WRF; green line), which shows a steady increase in the model differences with time going to peak values more than $10 \ m/s$ at $14.5 \ h$. The numerical diffusion signal following chaos (NUMAnoise - WRFnoise; red line) demonstrates random disturbances to the control but no systematic changes, as expected. This noise-perturbed curve represents the control curve's uncertainty envelope.

When we compare the differences between a noise-perturbed run and a noise-free run, we can determine the amplitude of the chaotic signal in each model. This model-specific chaotic signal for NUMA and WRF is depicted in Fig. 3.14 by the

purple and blue lines, respectively. The magnitude of both curves is significantly lower than the control simulation, represented by the green line. This is particularly true for WRF in that period that extends beyond the 12-hour mark, which is crucial when observational heating is implemented. These results show that the decrease in total vortex intensity seen in WRF was caused by implicit numerical dissipation (the "signal") is less chaotic than what happens when you change the beginning conditions with only a small amount of uncertainty. Also, because there is a lot of numerical dispersion in WRF, the "noise" simulation results in NUMA are much bigger than in WRF.

Chapter 4: Conclusions

4.1 Summary

By analyzing idealized simulations of the vortex reaction to time-dependent, 3D latent heating estimates derived from aerial radar measurements acquired during Hurricane Guillermo's(1997) RI, we have investigated the computational fluid dynamics of the RI process. Idealized heating perturbations were also examined, including a summation of low-order azimuthal wave numbers (0,2,3,4,5). Two kinds of the numerical model were considered: WRF, a community-based finite difference and split-explicit model, and NUMA, a state-of-the-art spectral element and semi-implicit model. To ensure that the differences can be pinned down to the numerical schemes that make up the dynamic core, the models are meticulously prepared and examined before use. The explicit diffusion parameters are parameterized based on the results of an experiment with a 3D TKE sub-grid model.

Studies have employed straightforward thermal perturbations to the starting conditions to depict the effects of convective heating in the past. Those studies have revealed that the WRF model has substantial implicit numerical dissipation when compared to leading research codes like NUMA [32]. Significant implicit numerical dissipation in WRF, characterized by a decline in numerous intensity measures over

a 6 h time, is also discovered in the present investigation. When the eddy diffusivity values are identical, the maximum wind speeds in WRF are about 12% lower than in NUMA. The time-integrated, mean kinetic energy values in WRF are close to 20% lower than in NUMA when differences in the Laplacian diffusion operator are taken into account, and the peak, localized wind speed differences in WRF are 12 m/s lower than in NUMA. Reed et al. [52] observed that the spectral element core generated the most intense storms in global hurricane simulations, implying that this numerical approach was the least diffusive. But their results are complicated because some dynamic cores use explicit diffusion mechanisms and coefficients that seem different from the others. This makes it hard to trace the differences in the solutions back to the numerical methods.

Extensive sensitivity analysis suggests that the explicit diffusion in WRF must be significantly reduced, with eddy viscosity values set to 50% of those in NUMA, to produce an intensity time series comparable to NUMA. This is necessary to acquire the same results as NUMA. The NUMA wind speeds are higher than the WRF wind speeds by roughly 5 meters per second when averaged across the eye-wall, with local spots exceeding 10 meters per second. In addition, when considering the increased values in the eye wall, the velocity gradients (as well as the Laplacian diffusion) are more significant in NUMA than in WRF. This is because the low wind zone in NUMA is slightly wider.

The more extended simulations incorporated both idealized and observed heating into the process. Even after 18 hours of simulation, WRF showed substantial overall reductions in vortex intensity, with large parts of the low-level eye-wall mov-

ing $10-20 \ m/s$ slower than NUMA for several hours. In the later rounds of the simulations, the models indicated slight disparities in other intensity measures, such as the highest azimuthal mean wind speed. This highlighted the necessity of accurately characterizing the whole vortex wind field. In the middle of the simulation that lasted for 18 hours, heating-induced meso-vortices in NUMA caused turbulent mixing between the eye and eye-wall of the vortex. However, this did not take place in WRF due to the effects of implicit numerical dissipation.

Comparisons were made between the models' azimuthal mean kinetic energy budgets to understand their discrepancies better. Throughout the 6-hour simulation, the pressure gradient force contributed much more to kinetic energy in NUMA than in WRF, ranging from an average of 23% to a high of 40%. When looking at the horizontal components of the pressure term, it can be shown that NUMA causes more extreme pressure gradient anomalies locally than WRF. The observed thermal inputs associated with these localized areas can be utilized to reconstruct the history of convective bursts, which often occur during the RI process. In addition, higher amplitudes in NUMA are observed for azimuthal waves in the pressure gradient term. This finding lends credence to the theory that these waves are born from Rossby motions in vortices. Even though the axisymmetric transport of kinetic energy, especially by vertical fluxes, is much larger than the asymmetric transport, it was discovered that these eddy processes contribute 15–40% at 30-minute output intervals over the 6-h period and 18% when integrating the terms over time. This was revealed even though the asymmetric transport is substantially smaller.

Multiple temporal integration methodologies were tested in NUMA's sensitiv-

ity analyses to identify the specific numerical parameters responsible for the model deviations. Switching from a first-order in-time approach to a second-order in-time strategy had no discernible effect on the NUMA solutions used for the control run. Instead, the outcomes were nearly comparable. In contrast to these findings, Guimond et al. [32] research revealed that higher-order temporal integration strategies resulted in even more robust solutions. Because the topic is so complicated, people will likely have different ideas about it. Guimond et al. [32] looked at moderate forcing in two dimensions in the previous study. This time, we looked at high forcing in four dimensions to learn more about how a vortex forms in response to a change. WRF's significant numerical dissipation is regulated by a spatial discretization mistake since it utilizes a second-order approximation to the pressure gradient force, while NUMA uses a fifth-order approximation. In contrast, NUMA employs a first-order approximation to the pressure gradient force.

The inevitable follow-up inquiry is, "Which model solution is correct?" Because this study is about idealized simulations, a numerical convergence analysis is the most appropriate tool for answering questions about this topic. WRF simulations with a horizontal grid spacing of 1 and 0.5 kilometers indicated an increase in vortex intensity (towards that of NUMA) along several metrics compared to the control run with a horizontal grid spacing of 2 kilometers. These results show that as more grid points are added to WRF, the mistakes associated with its implicit numerical dissipation are either alleviated or moved to lower scales. This is due to the incorporation of more grid points. However, WRF simulations at 0.5 kilometers show that the vortex's intensity has diminished (in comparison to NUMA). Com-

pared to NUMA, which has fifth-order spatial precision, WRF has second-order spatial accuracy due to pressure gradient discretization. This means that WRF would need to raise resolution in the x, y, and z dimensions by a factor of two (compared to the 2 km control) to approach the numerical inaccuracy in the 2 km NUMA simulations. The one-dimensional advection equation was used to produce these estimates. The convergence curves for the second-order and fifth-order numerical techniques are supplied in Giraldo et al. [40]. Making more grid changes in WRF, particularly in the vertical direction, may allow us to arrive at a more "right" answer (which was not investigated).

This work [53] revisits the introductory discussion of the core problem of significant low bias in RI circumstances in operational models. It suggests that implicit numerical dissipation may be to blame for some of the issues. Excessive numerical dissipation is not a desirable component of a modeling system since it reduces the simulations' effective resolution and can diminish the effects of physics-based sub-grid models and observations used to initialize the model in data assimilation approaches. The chaotic predictability horizon is a constant concern in nonlinear dynamical systems. Still, this uncertainty should represent a random mistake rather than the bias now seen for RI cases.

4.2 Future Work

There is still much research to be done to gain a better grasp of the consequences of computational physics of the RI process. This study's simulations only

considered dry dynamics, which means that the positive feedback loop that ordinarily connects wind speed, surface enthalpy fluxes, microphysical heating, and pressure anomalies was not included. As a result, there were no pressure abnormalities. When wet dynamics and other physical processes are considered, we predict significant model divergence, with the possibility of further WRF intensity reductions. This work provides the groundwork for a more in-depth investigation of the computational fluid dynamics of the hurricane RI process; nonetheless, more research is needed. Despite this, the work does a fantastic job of setting the stage.

The numerical dissipation can be controlled by employing a more refined SGS model. As data-driven SGS models incorporating Machine Learning (ML) gain popularity, most SGS modeling efforts are limited to the large eddy simulations (LES). Multiple academics have investigated the viability of using ML to develop SGS models for LES. [54,55]. Recent research has been mostly about improving SGS models for LES at the micro-scale and making simulations more reliable. However, we also need to pay special attention to energy transfer at the mesoscale. Data-driven SGS models outperformed their physics-based counterparts when simulating energy fluxes between scales. These data-driven models will accurately predict the interscale energy transfer using optimal data from storm simulations and machine/deep learning techniques.

Bibliography

- [1] T.R. Knutson, J.J. Sirutis, M. Zhao, R.E. Tuleya, M. Bender, G.A. Vecchi, G. Vollarini, and D. Chavas. Global projections of intense tropical cyclone activity for the late twenty-first century from dynamical downscaling of down-scaling of CMIP5/RCP4.5 scenarios. J. Climate, 28:7203-7224, 2015.
- [2] T. Knutson, S.J. Camargo, J.C.L. Chan, E. Kerry, H. Chang-Hoi, K. James, M. Mrutyunjay, S. Masaki, S. anf Masato, W. Kevin, and W. Liguang. Tropical cyclones and climate change assessment: part II. Projected Response to Anthropogenic Warming. *Bull. Am. Meteorol. Soc.*, 101:E303–E322, 2019.
- [3] Lin Li and Pinaki Chakraborty. Slower decay of landfalling hurricanes in a warming world. *Nature*, 587(7833):230—234, 2020.
- [4] F. Marks and L. Shay. Landfalling tropical cyclones: Forecast problems and associated research opportunities. Bulletin of the American Meteorological Society, 79:305–323, 1998.

- [5] E. Rappaport, J. Franklin, L. Avila, S. Baig, J. Beven, Eric S. Blake, Christopher A. Burr, Jiann-Gwo Jiing, C. A. Juckins, R. Knabb, C. Landsea, M. Mainelli, Max Mayfield, Colin J. McAdie, Richard J. Pasch, C. A. Sisko, S. R. Stewart, and Ahsha N. Tribble. Advances and challenges at the national hurricane center. Weather and Forecasting, 24:395–419, 2009.
- [6] M. DeMaria, C. Sampson, J. Knaff, and K. D. Musgrave. Is tropical cyclone intensity guidance improving. *Bulletin of the American Meteorological Society*, 95:387–398, 2014.
- [7] Mark DeMaria, James L. Franklin, Matthew J. Onderlinde, and John Kaplan.

 Operational forecasting of tropical cyclone rapid intensification at the national hurricane center. *Atmosphere*, 12(6), 2021.
- [8] Lloyd J. Shapiro and Huch E. Willoughby. The response of balanced hurricanes to local sources of heat and momentum. *Journal of Atmospheric Sciences*, 39(2):378 – 394, 1982.
- [9] Kerry Emanuel. An air-sea interaction theory for tropical cyclones. Part I: Steady-state maintenance. *JAS*, 43:585–604, 1986.
- [10] Sydney Sroka and S. R. Guimond. Organized kinetic energy backscatter in the hurricane boundary layer from radar measurements. *Journal of Fluid Mechan*ics, 924:A21, 2021.
- [11] J.D. Hoffman and S. Frankel. Numerical Methods for Engineers and Scientists, Second Edition,. Taylor & Francis, 2001.

- [12] William C. Skamarock and Joseph B. Klemp. A time-split nonhydrostatic atmospheric model for weather research and forecasting applications. *Journal of Computational Physics*, 227(7):3465 3485, 2008. Predicting weather, climate and extreme events.
- [13] A.G. Kravchenko and P. Moin. On the effect of numerical errors in large eddy simulations of turbulent flows. *Journal of Computational Physics*, 131(2):310– 322, 1997.
- [14] J. Larsson, S. Lele, and P. Moin. Effect of numerical dissipation on the predicted spectra for compressible turbulence. *Annual research briefs*, 2007.
- [15] Implicit Large Eddy Simulation: Computing Turbulent Fluid Dynamics. Cambridge University Press, 2007.
- [16] D.S. Abdi, L.C. Wilcox, T.C. Warburton, and F. X. Giraldo. A gpu-accelerated continuous and discontinuous galerkin non-hydrostatic atmospheric model. The International Journal of High Performance Computing Applications, 33(1):81– 109, 2017.
- [17] D.S. Abdi, F. X. Giraldo, Emil M Constantinescu, Lester E Carr, Lucas C Wilcox, and Timothy C Warburton. Acceleration of the implicit–explicit non-hydrostatic unified model of the atmosphere on manycore processors. *The International Journal of High Performance Computing Applications*, 33(2):242–267, 2019.

- [18] Z. J. Wang, K. Fidkowski, R. Abgrall, F. Bassi, D. Caraeni, A. Cary, H. Deconinck, R. Hartmann, K. Hillewaert, H. T. Huynh, N. Kroll, G. May, P.-O. Persson, B. van Leer, and Mi. Visbal. High-order cfd methods: current status and perspective. *International Journal for Numerical Methods in Fluids*, 72:811–845, 2013.
- [19] Albert E. Honein and Parviz Moin. Higher entropy conservation and numerical stability of compressible turbulence simulations. *Journal of Computational Physics*, 201(2):531–545, 2004.
- [20] G. J. Gassner and A. D. Beck. On the accuracy of high-order discretizations for underresolved turbulence simulations. *Theor. Comput. Fluid Dyn.*, 27:221—-237, 2013.
- [21] R.C. Moura, G. Mengaldo, J. Peiró, and S.J. Sherwin. On the eddy-resolving capability of high-order discontinuous Galerkin approaches to implicit LES / under-resolved DNS of euler turbulence. *Journal of Computational Physics*, 330:615–623, 2017.
- [22] G. Blaisdell, E. Spyropoulos, and J. Qin. The effect of the formulation of nonlinear terms on aliasing errors in spectral methods. *Applied Numerical Mathematics*, 21:207–219, 1996.
- [23] G. J. Gassner. A skew-symmetric discontinuous galerkin spectral element discretization and its relation to sbp-sat finite difference methods. SIAM Journal on Scientific Computing, 35:A1233–A1253, 2013.

- [24] G.-S. Karamanos and G. Karniadakis. A spectral vanishing viscosity method for large-eddy simulations. *Journal of Computational Physics*, 163:22–50, 2000.
- [25] P. F. Fischer and J. S. Mullen. Filter-based stabilization of spectral element methods. Comptes Rendus de l\(\hat{A}\)cad\(\epsilon\)mie des Sciences - Series I - Mathematics, 332:265–270, 2001.
- [26] P.-O. Persson and J. Peraire. Sub-cell shock capturing for discontinuous Galerkin methods. *Proc. of the 44th AIAA Aerospace Sciences Meeting and Exhibit*, AIAA-2006-112, 2006.
- [27] M. L. Yu, F. X. Giraldo, M. Peng, and Z. J. Wang. Localized Artificial Viscosity Stabilization of Discontinuous Galerkin Methods for Nonhydrostatic Mesoscale Atmospheric Modeling. *Monthly Weather Review*, 143:4823–4845, 2015.
- [28] Bernardo Cockburn and Chi-Wang Shu. The runge–kutta discontinuous galerkin method for conservation laws v: Multidimensional systems. *Journal of Computational Physics*, 141(2):199–224, 1998.
- [29] Jianxian Qiu and Chi-Wang Shu. Runge–Kutta Discontinuous Galerkin Method Using WENO Limiters. SIAM Journal on Scientific Computing, 26:907—-929, 2005.
- [30] X. Zhang and C.-W. Shu. On positivity preserving high order discontinuous galerkin schemes for compressible euler equations on rectangular meshes. J. Comput. Phys., 229:8918–8934, 2010.

- [31] Tetsuya Takemi and Richard Rotunno. The effects of subgrid model mixing and numerical filtering in simulations of mesoscale cloud systems. *Monthly Weather Review*, 131(9):2085 2101, 2003.
- [32] S. R. Guimond, Jon Reisner, Simone Marras, and F. X. Giraldo. The impacts of dry dynamic cores on asymmetric hurricane intensification. *Journal of the Atmospheric Sciences*, 73:4661 4684, 2016.
- [33] René Laprise. The euler equations of motion with hydrostatic pressure as an independent variable. Monthly Weather Review - MON WEATHER REV, 120, 1992.
- [34] J. Klemp and Robert Wilhelmson. The simulation of three-dimensional convective storm dynamics. *J. Atmos. Sci.*, 35:1070–1096, 1978.
- [35] Louis J. Wicker and William C. Skamarock. Time-Splitting Methods for Elastic Models Using Forward Time Schemes. Monthly Weather Review, 130(8):2088– 2097, 2002.
- [36] F. X. Giraldo and M. Restelli. A study of spectral element and discontinuous Galerkin methods for the Navier Stokes equations in nonhydrostatic mesoscale atmospheric modeling: Equation sets and test cases. *Journal of Computational Physics*, 227(8):3849–3877, 2008.
- [37] F. X. Giraldo, Marco Restelli, and Matthias Läuter. Semi-implicit formulations of the navier–stokes equations: Application to nonhydrostatic atmospheric modeling. SIAM J. Sci. Comput., 32:3394–3425, 2010.

- [38] James F. Kelly and F. X. Giraldo. Continuous and discontinuous Galerkin methods for a scalable three-dimensional nonhydrostatic atmospheric model: limited-area mode. *Journal of Computational Physics*, 231(24):7988–8008, 2012.
- [39] Francis X. Giraldo, James F. Kelly, and Emil M. Constantinescu. Implicit-explicit formulations of a three-dimensional nonhydrostatic unified model of the atmosphere (numa). SIAM J. Sci. Comput., 35, 2013.
- [40] F. X. Giraldo. An Introduction to Element-based Galerkin Methods on Tensor-Product Bases - Analysis, Algorithms, and Applications, volume 24. Springer, 2020.
- [41] David S Nolan and Lewis D Grasso. Nonhydrostatic, three-dimensional perturbations to balanced, hurricane-like vortices. part ii: Symmetric response and nonlinear simulations. *JAS*, 60(22):2717–2745, 2003.
- [42] MT Montgomery, ME Nicholls, TA Cram, and AB Saunders. A vortical hot tower route to tropical cyclogenesis. *Journal of the atmospheric sciences*, 63(1):355–386, 2006.
- [43] P. D. Reasor, M. D. Eastin, and J. F. Gamache. Rapidly intensifying Hurricane Guillermo (1997). Part I: Low-wavenumber structure and evolution. Mon. Wea. Rev., 137, 2009.

- [44] S. R. Guimond, G. M. Heymsfield, and F. J. Turk. Multiscale observations of Hurricane Dennis (2005): The effects of hot towers on rapid intensification. J. Atmos. Sci., 67, 2010.
- [45] R.F. Rogers, P.D. Reasor, and S. Lorsolo. Airborne doppler observations of the inner-core structural differences between intensifying and steady-state tropical cyclones. MWR, 141:2970–2991, 2013.
- [46] S. R. Guimond, M. A. Bourassa, and P. D. Reasor. A latent heat retrieval and its effects on the intensity and structure change of Hurricane Guillermo (1997).
 Part I: The algorithm and observations. J. Atmos. Sci., 68:1549–1567, 2011.
- [47] S. R. Guimond and J. M. Reisner. A latent heat retrieval and its effects on the intensity and structure change of Hurricane Guillermo (1997). Part II: Numerical simulations. J. Atmos. Sci., 69, 2012.
- [48] William C. Skamarock, Joseph B. Klemp, Jimy Dudhia, O. Gill, Zhiquan Liu, Judith Berner, Wei Wang, G. Powers, Greg Duda, Dale M. Barker, and Xiang yu Huang. A description of the advanced research wrf model version 4. NCAR Technical Notes, 2021.
- [49] Michael T. Montgomery and Janice Enagonio. Tropical cyclogenesis via convectively forced vortex rossby waves in a three-dimensional quasigeostrophic model. *Journal of the Atmospheric Sciences*, 55(20):3176 3207, 1998.
- [50] S. R. Guimond, Mark Bourassa, and Paul Reasor. A Latent Heat Retrieval and Its Effects on the Intensity and Structure Change of Hurricane Guillermo

- (1997). Part I: The Algorithm and Observations. *Journal of The Atmospheric Sciences J ATMOS SCI*, 68:1549–1567, 2011.
- [51] Myung-Sook Park and Russell L. Elsberry. Latent heating and cooling rates in developing and nondeveloping tropical disturbances during tcs-08: Trmm pr versus eldora retrievals. *Journal of the Atmospheric Sciences*, 70(1):15 – 35, 2013.
- [52] Kevin A. Reed and Christiane Jablonowski. Idealized tropical cyclone simulations of intermediate complexity: A test case for agcms. *Journal of Advances in Modeling Earth Systems*, 4(2), 2012.
- [53] M. B. Hasan, S. R. Guimond, M. L. Yu, S. Reddy, and F. X. Giraldo. The effects of numerical dissipation on hurricane rapid intensification with observational heating. *Journal of Advances in Modeling Earth Systems*, 14(8), 2022.
- [54] Corentin J. Lapeyre, Antony Misdariis, Nicolas Cazard, Denis P. Veynante, and Thierry Poinsot. Training convolutional neural networks to estimate turbulent sub-grid scale reaction rates. *Combustion and Flame*, 2019.
- [55] Andrea Beck, David Flad, and Claus-Dieter Munz. Deep neural networks for data-driven LES closure models. Journal of Computational Physics, 398:108910, 2019.